Faculty of Science
Palacký University
Olomouc

Measurement uncertainty of optical 3D sensors on optically smooth and rough surface

Pavel Pavlíček

Habilitation thesis

Olomouc 2021

Přírodovědecká fakulta
Univerzita Palackého
Olomouc

Nejistota měření optických 3D senzorů na opticky hladkém a drsném povrchu

Pavel Pavlíček

Habilitační práce

Olomouc 2021

Acknowledgements

I would like to thank all those who have contributed to the creation of this text. To my colleagues from the Joint Laboratory of Optics, to the coauthors of our articles and to my students.

Pavel Pavlíček

Declaration of originality

I hereby confirm that I am the sole author of the submitted thesis which, to the best of my knowledge and belief, contains no material previously published by another person, except where due acknowledgement has been made.

The author grants permission to Palacký University in Olomouc to store and display this thesis and its electronic version in the university library and on the official website.

Contents

Chapter 1

Introduction

The measurement of the geometric shape of different objects is an important task of metrology. For many years, the mechanical tactile sensors have been established in this field. Above all, their low measurement uncertainty and high reliability make their use the standard measuring method.

At present, the forces applied to the tips of the tactile sensors are so negligible that it is questionable, whether they should be still called contact measurement instruments. In addition, the mechanical tactile sensors show an excellent lateral resolution (Schmit et al., 2007).

However, also the mechanical tactile sensors have their limits. Their major disadvantage is the relatively long measurement time because they measure the shape of surface point by point. For a fast and permanent measurement, the mechanical scanning is not suitable. To solve this problem, non-contact measurement methods have been developed, of which the optical are of great importance. An optical device that measures the geometric shape of an object is called an optical 3D sensor.

Optical 3D sensors measure the geometric shape of objects by use of light. Usually, the value of a space or angle coordinate is measured as a function of other coordinates. The coordinate value is obtained from light intensity values that are recorded by the detector. The resultant intensity recorded by the detector is created by composing from individual contributions. The individual contributions come from different parts of the surface, which usually lie close to each other. The way of composing resultant intensity is mainly influenced by two factors: whether the light is coherent or incoherent and whether the surface is optically smooth or rough.

The meaning of the terms optically smooth and optically rough surface is explained in Chapter 2. Approximately one can say that a surface is regarded as being optically smooth for a specific instrument when the height variations within the resolution cell of the imaging system do not exceed plus/minus one-eighth of the wavelength of the light used. Similarly, a surface is regarded as being optically rough for a specific instrument when

its height variations within the resolution cell of the imaging system exceed plus/minus one-fourth of the wavelength of the light used (Häusler et al., 1999).

There are various methods for optical shape measurement. Some of them are suitable for the measurement of optically smooth surfaces, the paradigms are classical interferometry, phase measuring deflectometry, and confocal microscopy (Häusler, 1999; Häusler et al., 1999; Häusler and Ettl, 2011; Knauer et al., 2004). Optically rough surfaces are commonly measured by triangulation with a multitude of implementations, among them laser triangulation and phase measuring triangulation. Other methods suitable for the measurement of optically rough surfaces are focus search methods like shape from focus, point autofocus or focus variation (Häusler and Ettl, 2011; Nayar and Nakagawa, 1994). Only few methods are able to measure optically smooth and optically rough surfaces. The paradigm is coherence-scanning interferometry (CSI) (Dresel et al., 1992; Kino and Chim, 1990).

The value of the space or angle coordinate cannot be estimated absolutely accurately. The measurement result is affected by the measurement error. The reason why the shape of objects cannot be measured arbitrarily accurately is the ubiquitous noise. Chapter 3 explains what signal and noise are, how the measurement error is defined, and how the measurement uncertainty is determined. Cramér-Rao inequality is introduced as a suitable means of calculating measurement uncertainty [A1] (Pavlíček and Svak, 2015). In order to use Cramér-Rao inequality, we need to know the shape of the signal and the properties of the noise [A2, A3] (Pavlíček and Michálek, 2012a,b). The use of Cramér-Rao inequality is shown on the example of shot noise because of its significance in the case of optically smooth surfaces [A4] (Pavlíček and Hýbl, 2012).

When measuring the shape of an object with an optically smooth surface, shot noise is the dominant source of noise. The measurement uncertainty for some model measurement methods for optically smooth surface is calculated in Chapter 4 [A5] (Pavlíček and Pech, 2016). The spectral density quantity is introduced and its connection with the measurement uncertainty is explained [A6] (Pavlíček, 2014). The obtained results can also be applied to commonly used measurement methods such as classical interferometry and scanning microscopy [A5, A7] (Pavlíček and Pech, 2016; Pavlíček and Häusler, 2014).

In the case of measurement on optically rough surfaces, different sources of noise influence the measurement uncertainty. For example, the influence of surface roughness is the dominant source of noise in coherence-scanning interferometry on rough surface. Similarly, the speckle noise is the dominant source of noise in triangulation. The measurement uncertainty of coherence-scanning interferometry on rough surface is discussed in Chapter 5 as an example of the measurement uncertainty on optically rough surface. The origin of the signal and its evaluation is explained. The rough surface is

understood as a statistical set of scattering centers [A8] (Pavlíček and Soubusta, 2003). Based on statistical calculations, the measurement uncertainty is calculated [A9] (Pavlíček and Hýbl, 2008). The influence of spectrum width and roughness on the shape of the interferogram is investigated [A10] (Pavlíček, 2008).

Chapter 2

Optically smooth and optically rough surface

The coordinate value is determined from one or more intensity values recorded by the detector. The formation of the resultant intensity on the detector depends on whether the measured surface is optically smooth or optically rough (Häusler et al., 1999).

To understand the terms optically smooth and rough, let us first consider an imaging device that images the surface of the object in the image plane. For simplicity, let us assume that the absolute value of lateral magnification is equal to one and the point spread function has a width of Δ. Furthermore we assume that the light is spatially and temporally coherent and its wavelength is λ. The width of the point spread function defines the size of the lateral resolution cell.

If the heights of the individual scattering centers of the surface that are located within the resolution cell lie in the interval $(-\lambda/8, \lambda/8]$, then the phases of individual contributions lie in the interval $(-\pi/2, \pi/2]$. (Because of the reflection, the height difference $\lambda/8$ corresponds to the path difference $\lambda/4$ and thus to the phase difference $\pi/2$.) This means that the individual phasors add up constructively as shown by Argand diagram in Fig. 2.1(a) (Loudon, 2000). The intensity at each point of the image plane will be the result of constructive interference, no speckle pattern appears. Such a surface can be considered as an optically smooth surface.

If the heights located within the resolution cell exceed the interval $(-\lambda/4, \lambda/4]$, the phases of individual contributions fill uniformly the interval $(-\pi, \pi]$. This causes destructive interference between the individual phasors and a fully developed pattern appears in the image plane. The corresponding Argand diagram is illustrated in Fig. 2.1(b). Such a surface is considered as optically rough.

There is a transient range between optically smooth and optically rough surface. This applies to surfaces whose heights inside the resolution cell

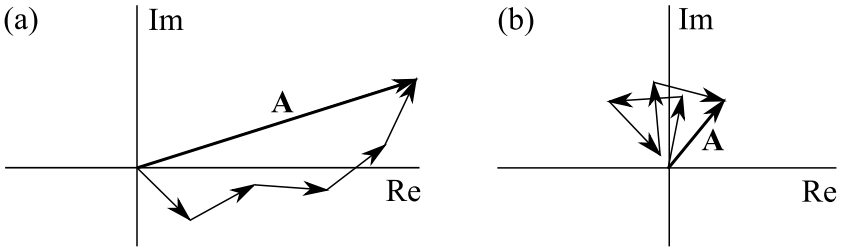

Figure 2.1: Argand diagram. (a) Optically smooth surface. (b) Optically rough surface.

exceed the interval $(-\lambda/8, \lambda/8]$ and do not exceed the interval $(-\lambda/4, \lambda/4]$ (Häusler et al., 1999).

An important conclusion is that the property of being optically smooth or optically rough does not only depend on the properties of the surface itself, but also on the properties of the imaging system and the wavelength of the light used (Häusler et al., 1999). However, the conditions under which the surface can be considered as optically smooth or optically rough can be determined more precisely.

2.1 Statistical properties of speckle pattern

Now, let us consider an imaging system consisting of two lenses. The schematic of the imaging system is illustrated in Fig. 2.2. The two lenses are positioned so that the back focal point of the first lens coincides with the front focal point of the second lens.

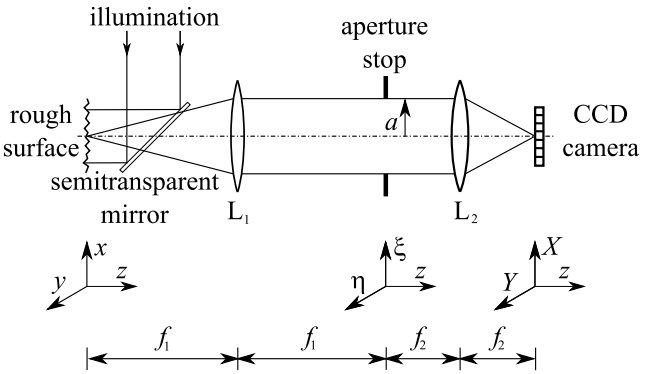

Figure 2.2: Schematic of two-lens imaging system.

First-order statistical properties of the speckle pattern generated by the two-lens imaging system are calculated in Goodman (1984). The statistical

properties we are interested in are mean values and variances of the real and imaginary parts of the field. However, the results presented in Goodman (1984) are derived on the assumption that the numerical aperture of the used lenses is low. In order not to be limited to small aperture lenses, we derive statistical properties without limitation to small apertures (Pavlíček, 2021).

The derivation is performed on the assumption that the illumination is monochromatic with wavelength λ and fully polarized. The rough surface, that is located in the front focal plane (x, y) of lens L_1, is illuminated by a plane wave. We assume that the height function $h(\,)$ describing the rough surface has normal distribution with zero mean and standard deviation σ_h. According to the definition, σ_h is equal to quadratic roughness Rq. A CCD detector is placed in the rear focal plane (X, Y) of lens L_2.

The phase of light in the object plane (x, y) is equal to

$$\vartheta_{\mathrm{i}}(x, y) = \frac{4\pi}{\lambda} h(x, y). \tag{2.1}$$

We can, without loss of generality, set the reflectivity and the incident intensity equal to unity (Goodman, 1984). The field at image coordinates (X, Y) is given by

$$A(X, Y) = \int_{-\infty}^{\infty} \int_{-\infty}^{\infty} dx\, dy\; K(X - M_{\mathrm{L}} x, Y - M_{\mathrm{L}} y) \exp[i\vartheta_{\mathrm{i}}(x, y)], \tag{2.2}$$

where $K(\,)$ is an amplitude weighting function and M_{L} is the lateral magnification. For the imaging system shown in Fig. 2.2, it holds $M_{\mathrm{L}} = -f_2/f_1$.

The form of the amplitude weighting function is determined by the form of the pupil function $k(\xi, \eta)$ in the pupil plane (ξ, η) (Goodman, 2005)

$$K(X, Y) = \frac{1}{\lambda^2 f_1 f_2} \int_{-\infty}^{\infty} \int_{-\infty}^{\infty} d\xi\, d\eta\; k(\xi, \eta) \exp\left[-i \frac{2\pi}{\lambda f_2} (\xi X + \eta Y)\right]. \tag{2.3}$$

It follows from Eq. (2.3) that the amplitude weighting function $K(\,)$ is equal to the Fourier transform of pupil function $k(\xi, \eta)$ divided by factor $\lambda^2 f_1 f_2$. The pupil function of a circular aperture with radius a is given by

$$k(\xi, \eta) = \mathrm{circ}\left[\frac{(\xi^2 + \eta^2)^{1/2}}{a}\right]. \tag{2.4}$$

The corresponding amplitude weighting function is equal to

$$K(X, Y) = \frac{\pi a^2}{\lambda^2 f_1 f_2} \times \frac{2\mathrm{J}_1\left[2\pi a (X^2 + Y^2)^{1/2} / (\lambda f_2)\right]}{2\pi a (X^2 + Y^2)^{1/2} / (\lambda f_2)}, \tag{2.5}$$

where $\mathrm{J}_1(\,)$ is the Bessel function of the first kind and first order.

The mean values of the real and imaginary parts of the field $A(X,Y)$ can be calculated from Eq. (2.2)

$$\langle A^{(r)}\rangle = \int_{-\infty}^{\infty}\int_{-\infty}^{\infty} dx\,dy\; K(X-M_{\mathrm{L}}x, Y-M_{\mathrm{L}}y)\langle\cos\vartheta_{\mathrm{i}}(x,y)\rangle, \quad (2.6)$$

$$\langle A^{(i)}\rangle = \int_{-\infty}^{\infty}\int_{-\infty}^{\infty} dx\,dy\; K(X-M_{\mathrm{L}}x, Y-M_{\mathrm{L}}y)\langle\sin\vartheta_{\mathrm{i}}(x,y)\rangle. \quad (2.7)$$

It holds for the mean values $\langle\cos\vartheta_{\mathrm{i}}(x,y)\rangle = \exp(-\sigma^2/2)$ and $\langle\sin\vartheta_{\mathrm{i}}(x,y)\rangle = 0$. The symbol σ denotes the standard deviation of the phase

$$\sigma = 4\pi\frac{\sigma_h}{\lambda}. \quad (2.8)$$

Thus

$$\langle A^{(r)}\rangle = -\frac{1}{M_{\mathrm{L}}}\exp\left(-\frac{1}{2}\sigma^2\right), \quad (2.9)$$

$$\langle A^{(i)}\rangle = 0. \quad (2.10)$$

The variances of the real and imaginary parts of the field $A(X,Y)$ are equal to

$$\sigma_r^2 = \frac{\exp(-\sigma^2)}{M_{\mathrm{L}}^2}\times \int_{-\infty}^{\infty}\int_{-\infty}^{\infty} d\Delta x\,d\Delta y\; \mathcal{K}(M_{\mathrm{L}}\Delta x, M_{\mathrm{L}}\Delta y)\{\cosh[\sigma^2 C(\Delta x,\Delta y)]-1\}, \quad (2.11)$$

$$\sigma_i^2 = \frac{\exp(-\sigma^2)}{M_{\mathrm{L}}^2}\times \int_{-\infty}^{\infty}\int_{-\infty}^{\infty} d\Delta x\,d\Delta y\; \mathcal{K}(M_{\mathrm{L}}\Delta x, M_{\mathrm{L}}\Delta y)\sinh[\sigma^2 C(\Delta x,\Delta y)]. \quad (2.12)$$

The symbol $\mathcal{K}(\,)$ denotes the autocorrelation function (Goodman, 1984)

$$\mathcal{K}(\alpha,\beta) = \int_{-\infty}^{\infty}\int_{-\infty}^{\infty} d\alpha'\,d\beta'\; K(\alpha',\beta')K(\alpha'-\alpha,\beta'-\beta), \quad (2.13)$$

$C(\,)$ is the normalized correlation function of the surface heights, $\Delta x = x - x'$, and $\Delta y = y - y'$.

In order to calculate the variations σ_r^2 and σ_i^2, it is necessary to know the shape of the autocorrelation function $\mathcal{K}(\,)$ and the normalized correlation function $C(\,)$. The autocorrelation function for the circular aperture is calculated by inserting from Eq. (2.5) into Eq. (2.13)

$$\mathcal{K}(X,Y) = \left(\frac{a}{\lambda f_1}\right)^2 \times \frac{2\mathrm{J}_1\left[2\pi a(X^2+Y^2)^{1/2}/(\lambda f_2)\right]}{2\pi a(X^2+Y^2)^{1/2}/(\lambda f_2)}. \tag{2.14}$$

According to Goodman (1984), we assume that the normalized correlation function of the surface heights has Gaussian form

$$C(r) = \exp\left[-\left(\frac{r}{r_c}\right)^2\right], \tag{2.15}$$

where $r = [(\Delta x)^2 + (\Delta y)^2]^{1/2}$ and r_c is surface correlation length (Whitehouse, 1994).

After inserting from Eqs. (2.14) and (2.15) into Eqs. (2.11) and (2.12), the approximate values of the variances can be calculated

$$\sigma_r^2 \approx \frac{\exp(-\sigma^2)}{M_\mathrm{L}^2}(\cosh\sigma^2 - 1) \times \left\{1 - \exp\left[-\frac{\mathrm{Chi}(\sigma^2) - \gamma - \ln\sigma^2}{N(\cosh\sigma^2 - 1)}\right]\right\}, \tag{2.16}$$

$$\sigma_i^2 \approx \frac{\exp(-\sigma^2)}{M_\mathrm{L}^2}\sinh\sigma^2 \times \left\{1 - \exp\left[-\frac{\mathrm{Shi}(\sigma^2)}{N\sinh\sigma^2}\right]\right\}. \tag{2.17}$$

Here, the symbols Chi( ) and Shi( ) denote the hyperbolic cosine and sine integrals, respectively, γ is Euler-Mascheroni constant ($\gamma \approx 0.577$), and the parameter N is defined by (Abramowitz and Stegun, 1970; Goodman, 1984)

$$N = \left(\frac{\lambda f_1}{\pi a r_c}\right)^2. \tag{2.18}$$

The physical meaning of the parameter N can be explained by means of speckle theory. The average diameter of a subjective speckle in the image plane (the plane with CCD in Fig. 2.2) is given by (Lauterborn et al., 1995)

$$D = 0.61\lambda\frac{f_2}{a}. \tag{2.19}$$

The diameter of a correlation cell is equal to $2r_c$. The correlation cell projected into the image plane has diameter $2M_\mathrm{L}r_c$. Thus, the number of correlation cells N_C that contribute to one speckle is given by

$$N_C = \left(\frac{D}{2M_\mathrm{L}r_c}\right)^2 = \left(\frac{0.61\lambda f_2}{2aM_\mathrm{L}r_c}\right)^2 = \left(\frac{\lambda f_1}{3.28\,ar_c}\right)^2 \approx N. \tag{2.20}$$

It follows from Eq. (2.20) that the parameter N represents the number of correlation cells that contribute to one speckle (Goodman, 1984).

The sought statistical parameters of the speckle pattern are expressed by Eqs. (2.9), (2.10), (2.16), and (2.17).

2.2 Phase distribution function

The knowledge of the statistical properties makes it possible to calculate the distribution function of the phase in the image plane (X, Y). The phase distribution function can be used as the sought criterion to distinguish whether the surface is optically smooth or rough.

For the case when the quantities $A^{(r)}$ and $A^{(i)}$ have a normal distribution, the phase distribution function has the following shape (Da Costa and Guerri, 1978)

$$p_\vartheta(\vartheta) = \frac{n\exp(-c)}{2\pi\alpha}\left\{1+\sqrt{\frac{\pi c}{\alpha}}\cos\vartheta\exp\left(\frac{c\cos^2\vartheta}{\alpha}\right)\times\right. \tag{2.21}$$

$$\left.\left[1+\operatorname{erf}\left(\sqrt{\frac{c}{\alpha}}\cos\vartheta\right)\right]\right\}.$$

The dimensionless parameters n, c, and α are given by

$$n = \frac{\sigma_r}{\sigma_i}, \tag{2.22}$$

$$c = \frac{[\langle A^{(r)}\rangle]^2}{2\sigma_r^2}, \tag{2.23}$$

$$\alpha = \frac{\sigma_i^2\cos^2\vartheta+\sigma_r^2\sin^2\vartheta}{\sigma_i^2}, \tag{2.24}$$

and erf( ) denotes the error function.

The phase distribution function described by Eq. (2.21) depends on three parameters $\langle A^{(r)}\rangle$, σ_r, and σ_i. If we take into account Eqs. (2.8), (2.9), (2.16), and (2.17), we find that the phase distribution function depends on only two parameters N and σ_h/λ. The value of lateral magnification M_L does not influence the shape of the phase distribution function. The parameters $\langle A^{(r)}\rangle$, σ_r, and σ_i are inversely proportional to M_L but only their mutual ratios occur in Eq. (2.21).

Thus, the statistical distribution of the phase in the image plane is a function of the parameters of both the object surface (σ_h and r_c) and the experimental setup (λ, a, and f_1).

For large values of the parameter N, the quantities $A^{(r)}$ and $A^{(i)}$ have a normal distribution. If the value of the parameter is lower (roughly $N < 0.2$), the shape of the distribution of quantities $A^{(r)}$ and $A^{(i)}$ deviates from the normal one. Nevertheless, numerical simulations show that even in this case the phase distribution is described by Eq. (2.21).

2.3 Optically smooth and rough surface

The calculated phase distribution $p_\vartheta(\vartheta)$ can be used as a criterion for whether the surface is optically smooth or rough.

The optically smooth surface is characterized by no destructive interference. Therefore, the surface is considered optically smooth if the phase distribution function $p_\vartheta(\vartheta)$ has nonzero value mainly in the interval $(-\pi/2, \pi/2]$ (range of constructive interference). It is expressed mathematically

$$\int_{-\pi/2}^{\pi/2} d\vartheta \, p_\vartheta(\vartheta) \geq 0.9973. \tag{2.25}$$

The numerical factor 0.9973 is chosen to comply the three sigma rule. An example of a phase distribution function for which the equality in Eq. (2.25) is satisfied is illustrated by the solid line in Fig. 2.3. In this case $N = 4$ and $\sigma_h/\lambda = 0.095$. It is clear from Fig. 2.3 that the main contribution to the phase distribution is given by the phase values from $-\pi/2$ to $\pi/2$.

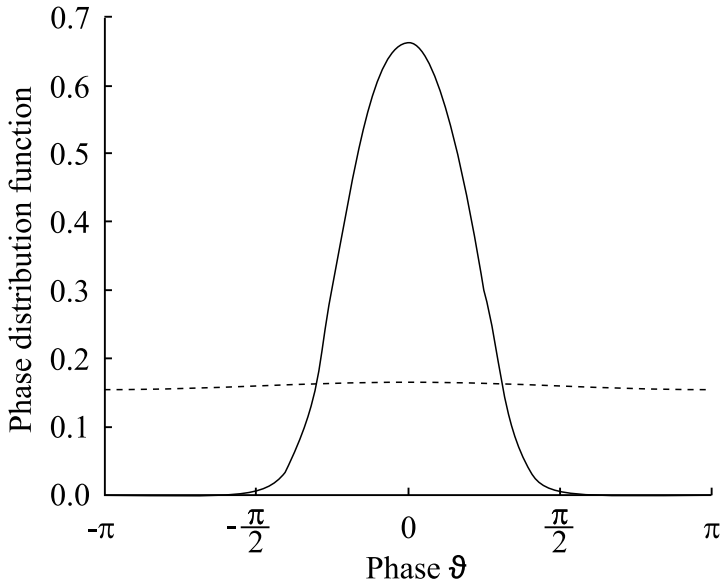

Figure 2.3: Phase distribution function for $N = 4$ and $\sigma_h/\lambda = 0.095$ (solid line) and $N = 4$ and $\sigma_h/\lambda = 0.270$ (dashed line).

A fully developed speckle pattern arises if the phase distribution is uniform in the interval $(-\pi, \pi]$. Thus, the limit is set so that the average value of the phase distribution function $p_\vartheta(\vartheta)$ in the interval $(-\pi/2, \pi/2]$ (range of constructive interference) is approximately the same as the average value of $p_\vartheta(\vartheta)$ in the interval $(-\pi, -\pi/2] \cup (\pi/2, \pi]$ (range of destructive interference).

N	$\frac{\sigma_h}{\lambda}$	$\frac{[\langle A^{(r)}\rangle]^2}{I}$	σ_ϑ
0.5	0.063	0.59	0.624
1	0.071	0.60	0.613
2	0.082	0.63	0.584
4	0.095	0.67	0.547
8	0.110	0.71	0.508
10	0.115	0.72	0.496
20	0.132	0.75	0.464
40	0.149	0.77	0.439

Table 2.1: Limit roughness values for optically smooth surface as function of number N of correlation cells.

A surface is considered optically rough if

$$\int_{-\pi}^{-\pi/2} d\vartheta\, p_\vartheta(\vartheta) + \int_{\pi/2}^{\pi} d\vartheta\, p_\vartheta(\vartheta) \geq 0.9545 \int_{-\pi/2}^{\pi/2} d\vartheta\, p_\vartheta(\vartheta). \tag{2.26}$$

The numerical factor 0.9545 is chosen because it matches the two-sigma rule. If Eq. (2.26) is satisfied, the phase distribution can be considered almost uniform. This is illustrated by the dashed line in Fig. 2.3. In this case $N = 4$ and $\sigma_h/\lambda = 0.270$.

The limit roughness values for optically smooth surface are listed in Table 2.1. The roughness value is expressed as ratio σ_h/λ. It is clear from the Table 2.1 that the limit roughness values depend on the number N of correlation cells. In addition, Table 2.1 shows intensity ratio $[\langle A^{(r)}\rangle]^2/I$ and standard deviation σ_ϑ of the phase in the image plane.

The expression $[\langle A^{(r)}\rangle]^2$ represents the intensity of the specular component. This intensity is compared with the total intensity I of the speckle (Goodman, 1984)

$$I = [\langle A^{(r)}\rangle]^2 + \sigma_r^2 + \sigma_i^2. \tag{2.27}$$

The ratio $[\langle A^{(r)}\rangle]^2/I$ is close to 1 for smooth surface. On the other hand it tends to 0 for rough surface.

N	$\frac{\sigma_h}{\lambda}$	$\frac{[\langle A^{(r)}\rangle]^2}{I}$	σ_ϑ
0.5	0.239	0.0004	1.793
1	0.248	0.0004	1.793
2	0.258	0.0004	1.794
4	0.267	0.0004	1.794
8	0.276	0.0004	1.794
10	0.279	0.0004	1.794
20	0.287	0.0004	1.794
40	0.295	0.0004	1.794

Table 2.2: Limit roughness values for optically rough surface as function of number N of correlation cells.

The value of standard deviation σ_ϑ of the phase ϑ is calculated from the phase distribution function

$$\sigma_\vartheta^2 = \int_{-\pi}^{\pi} d\vartheta \, p_\vartheta(\vartheta)\vartheta^2. \tag{2.28}$$

It is clear from Table 2.1 that the limit roughness for optically smooth surface takes values around one tenth of the wavelength. This is in agreement with Häusler et al. (1999), according to which the optically smooth surface is such that the height variances are below $\pm\lambda/8$.

The limit roughness values for optically rough surface are given in Table 2.2. Also here, the limit roughness values depend on the number N of correlation cells. Table 2.2 also shows the values of the ratio $[\langle A^{(r)}\rangle]^2/I$ and standard deviation σ_ϑ. It is clear that the intensity of the specular component is almost zero, as can be expected for a rough surface. For a completely rough surface, the phase distribution function is a constant function with the value $1/(2\pi)$. The standard deviation of such a function is $\pi/\sqrt{3} \approx 1.813$. The results given in Table 2.2 are close to this value.

One can see from Table 2.2 that the limit roughness for optically rough surface takes values around one fourth of the wavelength. According to Häusler et al. (1999), the height variations should be greater than $\pm\lambda/4$ for optically rough surface.

The meaning of the criteria defined by Eqs. (2.25) and (2.26) is explained in Fig. 2.4. The standard deviation σ_ϑ of the phase ϑ is plotted as a function of relative roughness σ_h/λ. The marks OS - T and T - OR indicate the transition from the optically smooth surface to the transient range and from the transient range to the optically rough surface, respectively.

The maximum value of the standard deviation is $\pi/\sqrt{3} \approx 1.813$, which corresponds to a continuous uniform distribution of ϑ from $-\pi$ to π.

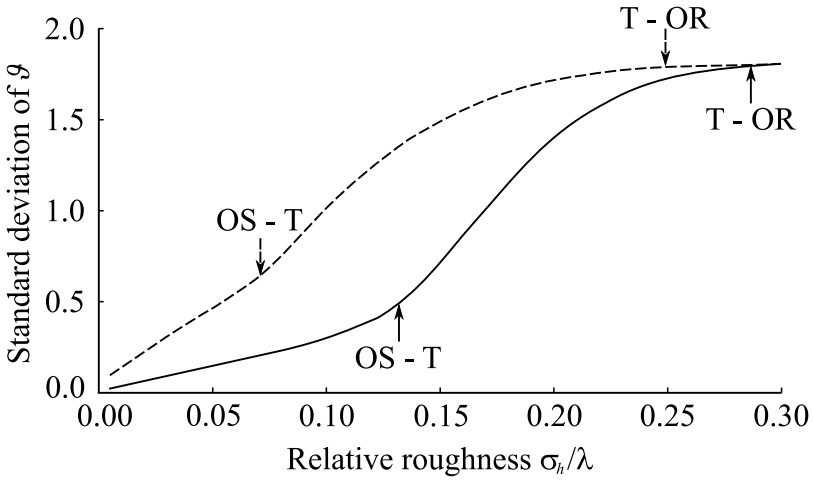

Figure 2.4: Standard deviation of phase ϑ as a function of relative roughness σ_h/λ. The graphs are plotted for two cases. 1) $f_1 = 80$ mm, $a = 2.8$ mm, $\lambda = 820$ nm ($N = 1$) (dashed line). 2) $f_1 = 358$ mm, $a = 2.8$ mm, $\lambda = 820$ nm ($N = 20$) (solid line). OS - T - transition from optically smooth surface to transient range, T - OR - transition from transient range to optically rough surface.

The limit roughness values are shown graphically in Fig. 2.5. The relative roughness σ_h/λ is plotted on the horizontal axis and the inverse of the number N is plotted on the vertical axis.

The curve AB represents the limit values for optically smooth surface as shown in Table 2.1. The limit values for the optically rough surface are illustrated by the curve EF according to Table 2.2. The area between the curves AB and EF represents the transient range (Häusler et al., 1999).

The quantity $1/N$ (and not N) is chosen because $1/N$ is proportional to the square of the numerical aperture of the lens L_1 [for small values of numerical aperture NA $= \lambda/(\pi r_c\sqrt{N})$]. Figure 2.5 shows that a surface with a certain roughness is optically smooth for a small numerical aperture value of L_1 (large N). However, the same surface ceases to meet the conditions for the optically smooth surface if the numerical aperture of L_1 increases (vertical movement up in the graph in Fig. 2.5). The increasing and decreasing of

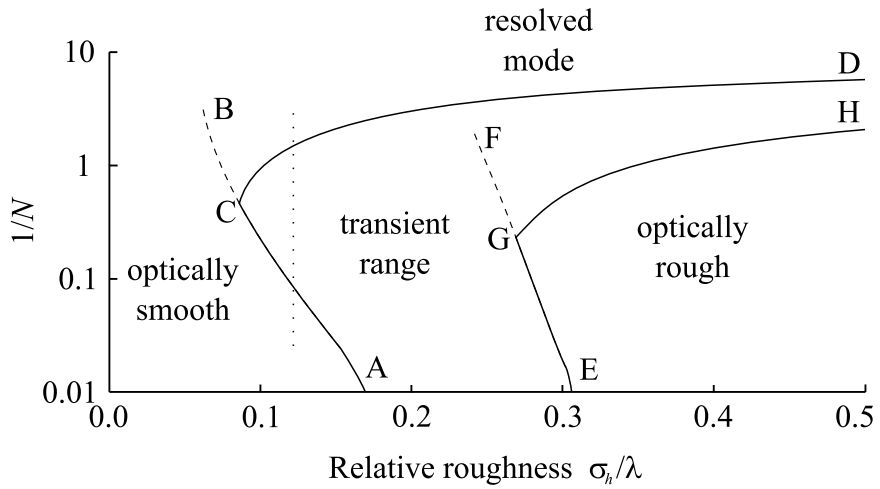

Figure 2.5: Limit roughness values for optically smooth and optically rough surface.

the numerical aperture of L_1 is shown by the vertical dotted line in Fig. 2.5.

The change of the surface correlation length r_c has a similar effect. If the other parameters do not change and the surface correlation length r_c increases, the initially optically smooth surface ceases to be optically smooth.

2.4 Transition between resolved and unresolved mode

As the numerical aperture of the lens L_1 increases, the resolution cell on the rough surface decreases. The unresolved mode switches to resolved mode. The transition from unresolved mode to resolved mode occurs when the numerical aperture of L_1 increases, even if the surface properties of the object do not change.

Effective roughness can be used as a criterion whether the surface is measured in resolved mode or unresolved mode. The effective roughness is defined as the roughness that is measured if we measure inside a single resolution cell only. The value of the effective roughness depends on the roughness and the surface correlation length as follows from Fig. 2.6.

The radius r_r of the resolution cell is equal to $r_r = 0.61\lambda f_1/a$. If the radius r_r decreases compared to the surface correlation length r_c, the effective roughness decreases. According to the definition, the effective roughness is given by

$$\sigma_e^2 = \frac{1}{A_{rc}} \int\limits_{A_{rc}} dx\, dy\; h^2(x,y), \tag{2.29}$$

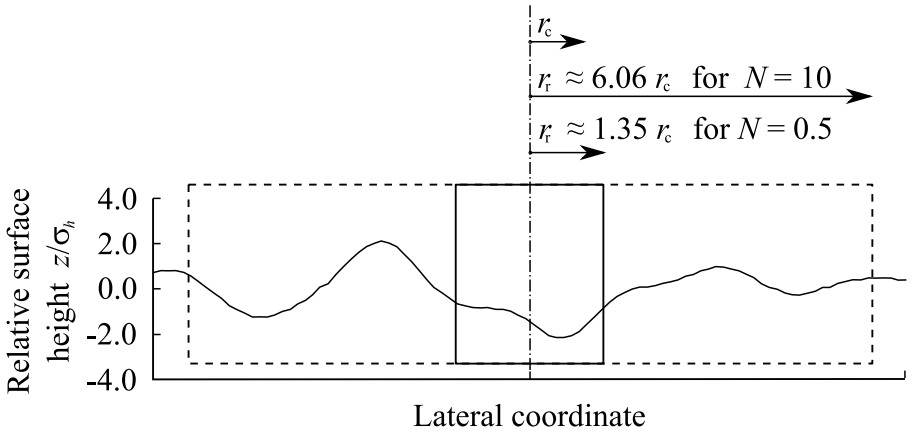

Figure 2.6: Influence of radius r_r on the value of effective roughness.

where A_{rc} is the area of the resolution cell.

The integral in Eq. (2.29) can be converted using Plancherel's theorem to

$$\int dx\, dy\; h^2(x,y) = \int d\nu_x\, d\nu_y\; |\mathcal{F}\{h(x,y)\}|^2, \tag{2.30}$$

where $\mathcal{F}$ denotes the Fourier transform and ν_x and ν_y are the spatial frequencies corresponding to the x and y coordinates, respectively. The integral to the right of Eq. (2.30) can be modified using the cross-correlation theorem

$$\int d\nu_x\, d\nu_y\; |\mathcal{F}\{h(x,y)\}|^2 = \int d\nu_x\, d\nu_y\; \mathcal{F}\{h(x,y) \star h(x,y)\}. \tag{2.31}$$

The symbol $\star$ denotes the cross-correlation.

Recall that a normalized correlation function is defined by (Whitehouse, 1994)

$$C(x,y) = \frac{1}{\sigma_h^2 A} h(x,y) \star h(x,y). \tag{2.32}$$

The symbol A means the area on which the normalized correlation function is calculated.

Substituting from Eqs. (2.30), (2.31), and (2.32) into Eq. (2.29), we obtain a relation for calculating the effective roughness

$$\sigma_e^2 = 2\pi\sigma_h^2 \int_{\rho_{\min}}^{\infty} d\rho\, \rho\, \mathcal{F}\{C\}. \tag{2.33}$$

Spatial frequency ρ is defined by $\rho^2 = \nu_x^2 + \nu_y^2$. The minimal spatial frequency $\rho_{\min}$ is related to the radius of the resolution cell $\rho_{\min} = 1/(2r_r)$.

We use the Gaussian form of the normalized correlation function [described by Eq. (2.15)] for the calculation. The Fourier transform of the normalized correlation function is equal to

$$\mathcal{F}\{C\} = \pi r_c^2 \exp[-(\pi \rho r_c)^2]. \tag{2.34}$$

Thus the effective roughness is equal to

$$\sigma_e = \sigma_h \exp\left[-\frac{1}{2}\left(\frac{\pi r_c}{2r_r}\right)^2\right] \approx \sigma_h \exp\left(-\frac{0.34}{N}\right). \tag{2.35}$$

We choose the limit for the resolved mode so that the effective roughness is the same as the limit roughness value for smooth surface and $N = 1$. This means that $\sigma_e/\lambda = 0.071$ as follows from Table 2.1. This condition defines curve CD in Fig. 2.5. The fully drawn curve ACD indicates the border of the optically smooth surface and resolved mode.

Similarly, the limit for the unresolved mode is set so that the effective roughness has the same value as the limit roughness value for rough surface and $N = 1$. Table 2.2 shows that $\sigma_e/\lambda = 0.248$. Curve GH in Fig. 2.5 is defined by this condition. The fully drawn curve EGH is the border of the optically rough surface and unresolved mode.

The area between curves ACD and EGH corresponds to the transient range.

Chapter 3

Influence of noise

A 3D sensor usually measures one coordinate of a point on the surface of the measured object. The measured coordinate value is expressed in relation to the other coordinates. Depending on the type of sensor, coordinate values of one or more points are measured. An example of such a measurement is shown in Tab. 3.1. In this example, z coordinate of 6 points is measured. The result of the measurement is the set of 6 values of the z coordinate measured in relation to the x and y coordinates.

x (set value)	y (set value)	z (measured value)
μm	μm	μm
0	0	10.1
0	10	10.4
0	20	10.6
10	0	8.2
10	10	8.3
10	20	8.5

Table 3.1: Example of a 3D measurement.

The measured *coordinate* value (the measurement result) is usually obtained by evaluation of a set of *intensity* values. As an example can be mentioned coherence scanning interferometry where one value of the z coordinate is obtained by the evaluation of an interferogram that may consist of several hundreds of intensity values (Dresel et al., 1992).

3.1 Signal

It has been mentioned above that the coordinate is determined from the intensity values. In fact, the detector measures the energy W of detected light

$$W = \eta I A T, \tag{3.1}$$

where η is the quantum efficiency, I is the intensity of light, A is the area of the detector, and T is the detection time. Equation (3.1) is valid provided that the intensity I is constant on area A over time T. Since the measured value W is proportional to the intensity, it will be called intensity in what follows. The whole set of values W_0, W_1,...,W_{M-1} is called a signal. The individual values W_0, W_1,...,W_{M-1} are also called samples. The number of samples is M.

The samples can be measured at one detector (e.g. a PIN diode) at subsequent time points. A typical example is the white-light interferogram recorded by a point sensor (Drabarek, 2001; Ulrich and Koch, 1992). Another possibility is that the samples are measured in various detectors (e.g. pixels of a line CCD camera) in one time point. A typical example is the signal of laser triangulation (Dorsch et al., 1994).

The searched coordinate value can be considered as a parameter of the acquired signal. Depending on the nature of the measurement, this may be, for example, the position of the maximum of the signal or the position of the center of gravity of the signal.

An example of a signal is shown in Fig. 3.1(a). The white bars indicate the individual intensity values W_i (the samples). Each intensity value W_i is assigned to a specific coordinate θ_i. In this example, the measured coordinate value is obtained as the position of the maximum of the signal. This position is denoted by θ_M and it is the searched parameter.

Since the sample values provide the only source of information, any estimate of the searched signal parameter must be some function of the samples $\{W_i\}$ (Riley et al., 2004). Such a function is called estimator.

However, the intensity values cannot be measured absolutely accurately because each measurement is affected by an error. The set of the individual errors is called noise. Thus, the measured signal is composed of the model signal and the noise [A3] (Pavlíček and Michálek, 2012b). The terms signal, model signal, and noise are explained in Fig. 3.1(b).

The white bars indicate the model signal. Model signal is the signal that would be obtained without the influence of the noise. The black bars indicate the noise. The resulting (measured) signal is indicated by the white rings.

Since the measured intensity values (samples) are affected by error, the searched parameter is also calculated with a certain error. This error is called measurement error. The cause of the measurement error is that the

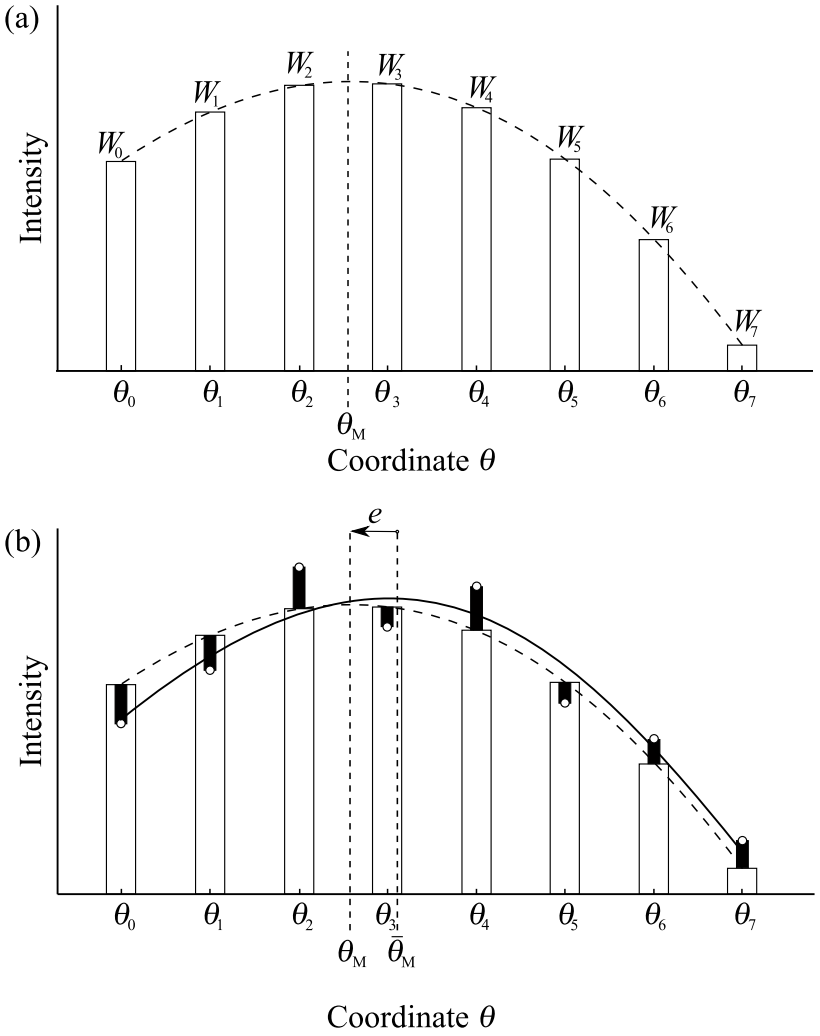

Figure 3.1: (a) Example of a signal. (b) Explanation of terms model signal (white bars - dashed line), noise (black bars), measured signal (white rings - solid line) and measurement error e ($e = \theta_M - \bar{\theta}_M$).

measured signal is evaluated instead of the model signal (which cannot be evaluated in principle). The measurement error is the error with which the coordinate is measured.

The measurement error should not be confused with the error that occurs when measuring individual samples [which is represented by black bars in Fig. 3.1(b)]. The meaning of the measurement error is explained in Fig. 3.1(b). The position of the maximum of the model signal is denoted by $\bar{\theta}_M$. The model signal is fitted by the dashed line. The position that is obtained as the maximum of the measured signal is denoted by θ_M. The

measured signal is fitted by the solid line. The measurement error e is equal to $e = \theta_M - \overline{\theta}_M$. The measurement error e is a random signed quantity. Its value is unknown.

Suppose we measure a signal several times in a row, the model signal of which is always the same. As a result, we measure a different signal each time, because noise is a random variable. Because the searched parameter is determined from the measured signal, each measurement gives a different result of the searched parameter. Thus, the searched parameter is also a random variable, we can determine its mean value and variance.

In general, we get different values of variance if we use different estimators. An estimator is called more efficient if the variance of the result is lower and less efficient if the variance is higher. However, the variance cannot be arbitrarily small. The variance cannot go below a certain limit. This limit can be calculated using Cramér-Rao inequality (Albrecht et al., 2003).

According to Guide to expression of uncertainty in measurement (2016), measurement uncertainty is a parameter that describes the dispersion of the measurement error. Thus, the measurement uncertainty can be identified with the standard deviation of the signal parameter being sought. Note that the standard deviation is the square root of variance.

Thus, the Cramér-Rao inequality is a suitable mathematical tool to determine the measurement uncertainty [A1] Pavlíček and Svak (2015). Two items of information need to be known for the application of the Cramér-Rao inequality:

- the analytical description of the model signal,
- the probability density function of the noise.

Because of the second point, an important task is to know the dominant source of noise. As for optical 3D sensors, the major sources of the noise are: the random arrival of photons at the detector (shot noise) and coherent noise (speckle pattern). These two sources are fundamental, although it may happen that other sources of noise (e.g. optical aberrations, mechanical vibrations, electronic noise, light source instabilities, positioning errors, quantization noise) become dominant (Pavlíček and Häusler, 2014).

The analytical expression of the model signal is assumed in the form

$$W_{mi} = W_m(\theta_i, a) \quad \text{for} \quad i = 0, 1, \ldots, M-1, \tag{3.2}$$

where W_m is an analytically described function and a is the searched parameter of the model signal.

For practical reasons, it is advantageous to divide the intensity dependence on the coordinate into a constant W_{mc} (with dimension of energy) and a dimensionless function $g(\,)$

$$W_{mi} = W_m(\theta_i, a) = W_{mc}\, g(\theta_i, a) \quad \text{for} \quad i = 0, 1, \ldots, M-1. \tag{3.3}$$

The measurement uncertainty depends on the shape of the model signal, the intensity and characteristics of the noise, and the estimator (algorithm) used. In practice, this means that the measurement uncertainty depends on the geometric arrangement of the optical 3D sensor, on the light source and its intensity, and the detector and its sensitivity (Ronchi, 1961).

3.2 Cramér-Rao inequality

The Cramér-Rao inequality expresses a lower bound on the variance of an estimator of a deterministic parameter. A parameter is called deterministic if it is fixed but unknown.

In our case, the parameter is the searched value of spatial coordinate. The determined lower bound represents a lower limit of the square of measurement uncertainty. Thus, the Cramér-Rao inequality makes it possible to calculate the minimum achievable measurement uncertainty [A4, A2] (Pavlíček and Hýbl, 2012; Pavlíček and Michálek, 2012a).

The Cramér-Rao inequality states that the variance of any unbiased estimator is at least as high as the inverse of the Fisher information J

$$\sigma_a^2 \geq \frac{1}{J}. \tag{3.4}$$

An estimator is called unbiased if its expectation value is equal to the true value. For practical computation of the parameters, the least-squares method can be used. The least squares method is generally a biased estimator. Nevertheless, the least-squares method can be considered as an unbiased estimator when the standard deviation of the noise is small in comparison with the amplitude of the signal (Kubáček, 1988).

The Fisher information is given by

$$J = \mathrm{E}\left[\left(\frac{\partial \ln p(\theta, a)}{\partial a}\right)^2\right], \tag{3.5}$$

where $p(\theta, a)$ is the joint probability density function and E[ ] denotes the expected value related to the distribution. The particular shape of the joint probability density function $p(\theta, a)$ depends on the analytical description of the model signal and the probability density function of the noise.

The method of calculating the measurement uncertainty is shown using an example of shot noise.

3.3 Cramér-Rao inequality for shot noise

Shot noise describes the fluctuations of the number of detected photons. Mathematically, shot noise is described by Poisson distribution. The prob-

ability density for discrete value y_i is given by (Vencálek, 2018)

$$p(y_i, a) = \frac{\lambda_i^{y_i}}{y_i!} \exp(-\lambda_i), \tag{3.6}$$

where y_i is the measured value of the intensity (in photocounts) and λ_i represents the value of the model signal (in photocounts). The quantities y_i and λ_i can be expressed

$$y_i = \frac{W_i}{h\nu}, \tag{3.7}$$

$$\lambda_i = \frac{W_{mi}}{h\nu} = \frac{W_m(\theta_i, a)}{h\nu}, \tag{3.8}$$

where h is Planck constant and ν is the frequency of light. Comparing Eq. (3.8) to Eq. (3.3), we see that $\lambda_i = g(\theta_i, a)$ and $W_{mc} = h\nu$.

We assume that the individual measurements are independent. Then, the joint probability density function is equal to the product of probability densities in all points $0 \dots M-1$.

$$p(y, a) = \prod_{i=0}^{M-1} p(y_i, a) = \prod_{i=0}^{M-1} \frac{\lambda_i^{y_i}}{y_i!} \exp(-\lambda_i). \tag{3.9}$$

The Fisher information is calculated by substituting the joint probability function from Eq. (3.9) into Eq. (3.5). The partial derivative of the logarithm of the joint probability density function is equal

$$\frac{\partial \ln p(y, a)}{\partial a} = \sum_{i=0}^{M-1} \left(y_i \frac{\lambda_i'}{\lambda_i} - \lambda_i' \right), \tag{3.10}$$

where λ_i' is the partial derivative of the model signal according to a

$$\lambda_i' = \left[\frac{\partial g(a, \theta)}{\partial a} \right]_{\theta=\theta_i}. \tag{3.11}$$

The square of the expression on the left hand side of Eq. (3.10) is calculated

$$\begin{aligned} \left(\frac{\partial \ln p(y, a)}{\partial a} \right)^2 &= \sum_{i=0}^{M-1} \left(y_i \frac{\lambda_i'}{\lambda_i} - \lambda_i' \right)^2 + \\ &+ \sum_{i=0}^{M-1} \sum_{j=0,\ j\neq i}^{M-1} \left(y_i \frac{\lambda_i'}{\lambda_i} - \lambda_i' \right) \left(y_j \frac{\lambda_j'}{\lambda_j} - \lambda_j' \right). \end{aligned} \tag{3.12}$$

In calculating the expected value, it is used that it holds

$$\mathrm{E}[y_i] = \lambda_i, \tag{3.13}$$

$$\mathrm{E}[y_i^2] = \lambda_i(\lambda_i + 1). \tag{3.14}$$

We substitute from Eq. (3.12) to Eq. (3.5) and use Eqs. (3.13) and (3.14)

$$J = \mathrm{E}\left[\left(\frac{\partial \ln p(\theta, a)}{\partial a}\right)^2\right] = \sum_{i=0}^{M-1} \frac{\lambda_i'^2}{\lambda_i}. \tag{3.15}$$

Since $\lambda_i = g(a, \theta_i)$, Fisher information is equal to

$$J = \sum_{i=0}^{M-1} \left[\frac{\partial g(a, \theta)}{\partial a}\right]^2_{\theta=\theta_i} \frac{1}{g(a, \theta_i)}. \tag{3.16}$$

We calculate the value of the lower limit of the measurement uncertainty by substituting the result of Eq. (3.16) into Eq. (3.4).

3.4 Summary

The noise causes measurement uncertainty. The terms signal, model signal and noise have been explained. Cramér-Rao inequality has been introduced as a means of calculating the measurement uncertainty. Because shot noise plays an important role in optics, the shape of Cramér-Rao inequality has been calculated for this type of noise. This chapter is based on publications:

[A1] Pavlíček, P. and V. Svak (2015). Noise properties of Hilbert transform evaluation. *Measurement Science and Technology 26*(8), 085207.

[A2] Pavlíček, P. and V. Michálek (2012a). White-light interferometry–envelope detection by Hilbert transform and influence of noise. *Optics and Lasers in Engineering 50*(8), 1063—1068.

[A3] Pavlíček, P. and V. Michálek (2012b). White-light interferometry, Hilbert transform, and noise. In *SPIE 8697*, pp. 86970B.

[A4] Pavlíček, P. and O. Hýbl (2012). White-light interferometry on rough surfaces——measurement uncertainty caused by noise. *Applied Optics 51*(4), 465—473.

Chapter 4

Measurement uncertainty on optically smooth surfaces

As mentioned in Chapter 3, the shot noise will be considered as the dominant source of noise if the shape of an object with optically smooth surface is measured. This approach makes it possible to compare the ultimate measurement uncertainty of various optical 3D measurement methods [A5] (Pavlíček and Pech, 2016).

The shot noise originates from the particle nature of light. The relationship between the variance $(\Delta N)^2$ in the photocount number and the mean photocount number $\langle N \rangle$ is given by the Poisson distribution (Fox, 2006)

$$(\Delta N)^2 = \langle N \rangle. \tag{4.1}$$

If we measure the value of coordinate θ and know the analytical form of the model signal $g(\,)$ then the lower limit δa of measurement uncertainty is calculated from the Cramér-Rao inequality

$$(\delta a)^2 \geq \left\{ \sum_{i=0}^{M-1} \left[\left(\frac{\partial g(a,\theta_i)}{\partial a} \right)^2_{\theta=\theta_i} \frac{1}{g(a,\theta_i)} \right] \right\}^{-1}. \tag{4.2}$$

Equation (4.2) is the result of substituting Eq. (3.16) into Eq. (3.4). Note that function $g(\,)$ is expressed in photocounts.

Then, the number N_{all} of photocounts detected in all samples is equal to

$$N_{\mathrm{all}} = \sum_{i=0}^{M-1} g(a,\theta_i). \tag{4.3}$$

Therefore Eq. (4.2) can be rewritten to

$$(\delta a)^2 \geq \frac{\sum_{i=0}^{M-1} I(a,\theta_i)}{N_{\mathrm{all}} \sum_{i=0}^{M-1} \left[\left(\frac{\partial I(a,\theta_i)}{\partial a} \right)^2_{\theta=\theta_i} \frac{1}{I(\theta_i,a)} \right]}. \tag{4.4}$$

The advantage of writing the Cramér-Rao inequality in the form given by Eq. (4.4) is that the intensity I can be expressed in arbitrary units because $I(\,) \propto g(\,)$. If the number M of samples is high, it is convenient to replace the sums in Eq. (4.4) by integrals [A7] (Pavlíček and Häusler, 2014)

$$(\delta a)^2 \geq \frac{\int\limits_{-\infty}^{\infty} d\theta I(a,\theta)}{N_{\text{all}} \int\limits_{-\infty}^{\infty} d\theta [I'(a,\theta)]^2 / I(a,\theta)}, \tag{4.5}$$

where $I'(a,\theta)$ is the partial derivative of function $I(a,\theta)$ with respect to a.

The result represented by Eq. (4.5) coincides with the result of Falconi (1964) who derived it for the angular position being the measured parameter. The meaning of Eq. (4.5) becomes clear below, when applied to particular measurement methods.

The shape of the object is measured by processing and evaluating the signal as described in Chapter 3. It turns out that one plane wave is not enough to generate a usable signal. Some possibilities how to obtain a signal that can be used for the measurement of the shape are described in the following text.

4.1 Two-slit device

An idealized measurement device that uses two plane waves is shown in Fig. 4.1. The measurement device is inspired by that described by Falconi (1964). A screen with two slits is located in the front focal plane of a lens with focal length f. The distance between the slits amounts to $2u$. Behind the lens, two plane waves with wave vectors $\mathbf{k}_1$ and $\mathbf{k}_2$ propagate and impinge on the surface of the measured object. The components of wave vectors are given as follows $\mathbf{k}_1 = (-k_{x0}, 0, k_{z0)})$ and $\mathbf{k}_2 = (k_{x0}, 0, k_{z0})$. The light reflects from the surface and propagates to a CCD line detector.

First, it is assumed that the object surface is perpendicular to the z-axis. Because of the interference of the two plane waves, a typical cosinusoidal interference pattern forms on the detector. The intensity distribution along the x-axis is illustrated by solid line in Fig. 4.2(a). Mathematically, the intensity distribution is expressed by

$$I(x) = I_0[1 + \cos(2k_{x0}x)], \tag{4.6}$$

where I_0 is mean intensity of the pattern.

If the surface is tilted by angle α around the y-axis, the interference pattern moves by distance x_0. The intensity distribution changes to

$$I(x) = I_0\{1 + \cos[2k_{x0}(x - x_0)]\}. \tag{4.7}$$

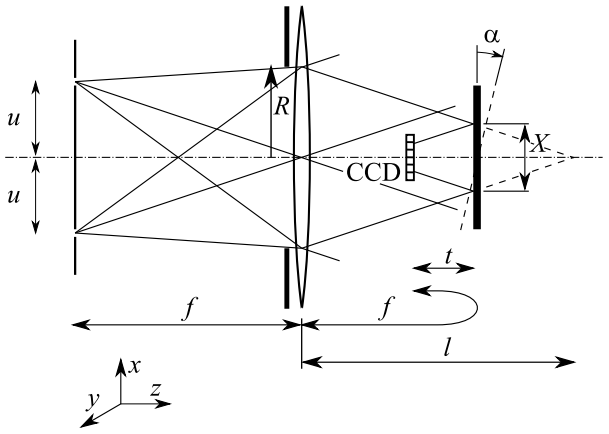

Figure 4.1: Schematic of two-slit device.

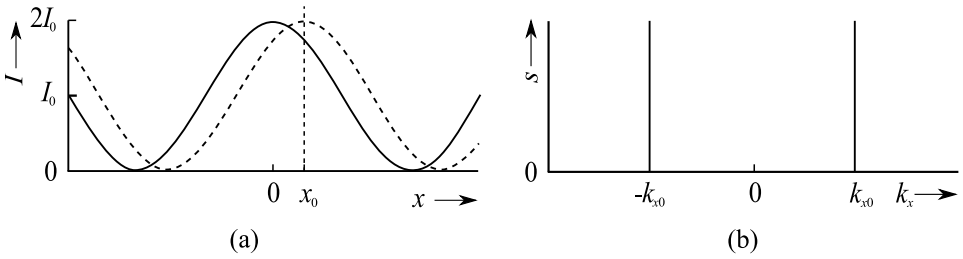

Figure 4.2: Two-slit device: (a) model signal, (b) normalized spectral density.

The changed intensity distribution is illustrated by dashed line in Fig. 4.2(a).

The intensity distribution on the detector represents the signal of the measurement device. From the change of the signal, the angle α of tilt can be determined. For small angles, it holds

$$x_0 = 2\alpha t, \tag{4.8}$$

where t is the distance between the mirror and the CCD. Thus, the described device is a simple model of a deflectometer.

The measurement uncertainty δx_0 can be calculated using Eq. (4.5). The shift x_0 plays the role of parameter a.

$$\delta x_0 = \frac{1}{2k_{x0}\sqrt{N_{\text{all}}}}. \tag{4.9}$$

The normalized spectral density s of the lateral component k_x of vector $\mathbf{k}$ is given by

$$s(k_x) = \frac{1}{2}[\delta(k_x + k_{x0}) + \delta(k_x - k_{x0})]. \tag{4.10}$$

The graph of the distribution is shown in Fig. 4.2(b). The lateral component of vector $\mathbf{k}$ takes two possible values: k_{x0} and $-k_{x0}$ both with the same relative appearance. The standard deviation of the lateral component k_x is equal to

$$\delta k_x = k_{x0}. \tag{4.11}$$

By the combination of Eqs. (4.9) and (4.11), the uncertainty product is obtained [A6] (Pavlíček, 2014)

$$\delta x_0 \cdot \delta k_x = \frac{1}{2\sqrt{N_{\text{all}}}}. \tag{4.12}$$

It follows from Eq. (4.12) that the uncertainty product depends only on the number N_{all} of photons used for the measurement.

The uncertainty of angle α follows from Eq. (4.8)

$$\delta\alpha = \frac{\delta x_0}{2t}. \tag{4.13}$$

The lateral size X of the area on which both waves overlap can be expressed by

$$X = 2(R - u) + \frac{2tu}{f} \tag{4.14}$$

and R is the radius of the aperture. The minimum size X_{min} for which the interference can be observed on the CCD is given by the condition $R = u$. Thus the minimum size is given by

$$X_{\text{min}} = \frac{2tu}{f}. \tag{4.15}$$

For small angles of wave propagation ($k_{x0} \ll k_{z0}$), it holds $k_{x0} = 2\pi u/(\lambda f)$. The uncertainty product for the uncertainty $\delta\alpha$ and minimum size X_{min} can be calculated from Eqs. (4.13) and (4.15)

$$\delta\alpha \cdot X_{\text{min}} = \frac{\lambda}{4\pi\sqrt{N_{\text{all}}}}. \tag{4.16}$$

The measurement uncertainty $\delta\alpha$ depends on the wavelength λ of the light, the size X_{min}, and the number N_{all} of photons. It is noteworthy that the measurement uncertainty $\delta\alpha$ does not depend on the distance between the measured surface and the CCD detector. The size X_{min} can be considered as the lateral resolution distance on the measured surface. Note that the distance l does not occur in Eq. (4.16). The result described by Eq. (4.16) is identical with that of Falconi (1964).

4.2 Two-slit device for z-direction

In order to measure in the z-axis direction, various values of the component k_z are necessary. This condition is not met on the two-slit device as described in Section 4.1. However, it is possible to modify the two-slit device so that the measurement in the z-axis direction is possible. The arrangement is presented in Fig. 4.3. The slits have form of two concentric circles with radii R_1 and R_2, respectively. The components of wave vectors are given by $\mathbf{k}_1 = (k_{x1}, k_{y1}, k_{z1})$ and $\mathbf{k}_2 = (k_{x2}, k_{y2}, k_{z2})$ with $k_{x1}^2 + k_{y1}^2 + k_{z1}^2 = k_{x2}^2 + k_{y2}^2 + k_{z2}^2$ and $k_{z2} \neq k_{z1}$. The light reflects from the measured object and propagates to a photodetector.

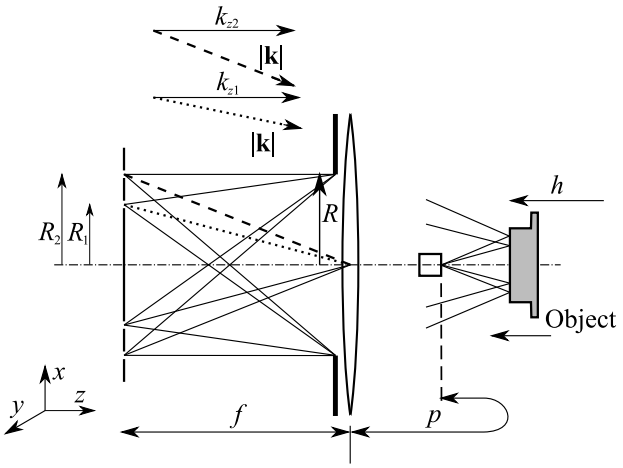

Figure 4.3: Schematic of two-slit device for z-axis direction.

The described device is a model of optical focus sensor (Schmit et al., 2007). It can measure the height h of the object. The measured object moves along the optical axis during the measurement process as indicated by the arrow in Fig. 4.3. If the object moves, the path length p changes. We assume that the intensity in both slits is the same. The amplitude function is given by

$$A(p) \propto \sqrt{I_0}\{\exp[ik_{z1}(p - p_0)] + \exp[ik_{z2}(p - p_0)]\}. \tag{4.17}$$

The sought quantity is the parameter p_0 from which the height h of the object can be determined $h = p_0/2$. The longitudinal components k_{z1} and k_{z2} are equal to $k_{z1} = (2\pi/\lambda)[1 - R_1^2/(2f^2)]$ and $k_{z2} = (2\pi/\lambda)[1 - R_2^2/(2f^2)]$, respectively. The measured signal is the intensity at the detector

$$I(p) = |A(p)|^2 \propto I_0\{1 + \cos[(k_{z1} - k_{z2})(p - p_0)]\}. \tag{4.18}$$

Graphically it is illustrated in Fig. 4.4(a). The measurement uncertainty δp_0 is obtained after inserting into Eq. (4.5).

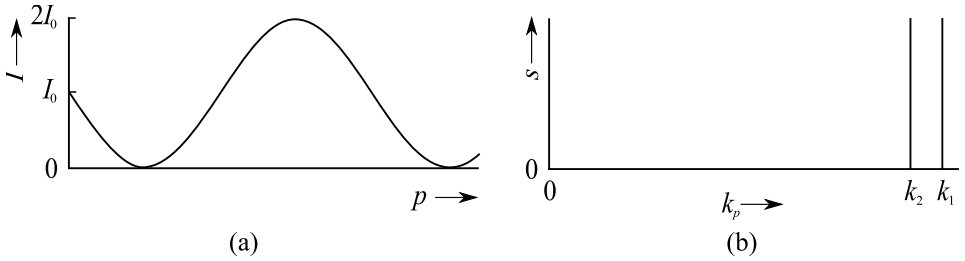

Figure 4.4: Two-slit device for z-axis direction: (a) model signal, (b) normalized spectral density.

$$\delta p_0 = \frac{1}{(k_{z1} - k_{z2})\sqrt{N_{\text{all}}}} = \frac{\lambda}{\pi\sqrt{N_{\text{all}}}} \frac{f^2}{R_1^2 - R_2^2}. \tag{4.19}$$

The normalized spectral density of the longitudinal component k_p of vector $\mathbf{k}$ is given by

$$s(k_p) = \frac{1}{2}[\delta(k_p - k_{z2}) + \delta(k_p - k_{z1})]. \tag{4.20}$$

The graph of the normalized spectral density is shown in Fig. 4.4(b). The standard deviation of k_p is $\delta k_p = (k_{z1} - k_{z2})/2$. After combining this result with Eq. (4.19), the uncertainty product appears

$$\delta p_0 \cdot \delta k_p = \frac{1}{2\sqrt{N_{\text{all}}}}. \tag{4.21}$$

The result of this uncertainty product is identical with that of Eq. (4.12).

Classical interferometry can also be considered as a special case of this arrangement. It is formed by two rays in opposite directions ($k_{z1} = k_0$, $k_{z2} = -k_0$) (Pavlíček and Häusler, 2014; Pavlíček and Pech, 2016). In this case, the measured signal is the dependence of the intensity I on the positions z_1 and z_2 of the mirrors

$$I = I_0\{1 + \cos[2k_0(z_2 - z_1)]\}. \tag{4.22}$$

Note the variance of the wave number occurs due to the different light ray directions, while the laser wavelength is fix. This explains the lower measurement uncertainty for classical interferometry in comparison with that for confocal microscopy. The variance of the wave vector components is maximized in a classical interferometry setup (two rays with opposite directions) (Fischer, 2019).

4.3 Device with a general shape aperture

The devices mentioned in Sections 4.1 and 4.2 are special cases of a device with a general shape aperture.

For the lateral direction, the amplitude function is equal to

$$A(x) \propto \int_{\mathcal{A}} d\xi \, d\eta \, \exp\left[i\frac{2\pi}{\lambda}\frac{\xi}{f}(x - x_0)\right], \tag{4.23}$$

where $\mathcal{A}$ is the aperture and ξ and η are the lateral coordinates in the aperture plane.

For the longitudinal direction, the amplitude function is given by

$$A(p) \propto \exp\left[i\frac{2\pi}{\lambda}(p - p_0)\right] \int_{\mathcal{A}} d\xi \, d\eta \, \exp\left[-i\frac{2\pi}{\lambda}\frac{\xi^2 + \eta^2}{2f^2}(p - p_0)\right]. \tag{4.24}$$

The amplitude function is calculated for circular aperture as an example. The aperture $\mathcal{A}$ is a disk with radius a. According to Eq. (4.24), the amplitude function is equal to

$$A(p) \propto \frac{1}{2}a^2 \exp\left[i\frac{2\pi}{\lambda}\left(1 - \frac{a^2}{4f^2}\right)(p - p_0)\right] \operatorname{sinc}\left[\frac{2\pi}{\lambda}\frac{a^2}{4f^2}(p - p_0)\right]. \tag{4.25}$$

The corresponding intensity function has the form

$$I(p) \propto \frac{1}{4}a^4 \operatorname{sinc}^2\left[\frac{2\pi}{\lambda}\frac{a^2}{4f^2}(p - p_0)\right]. \tag{4.26}$$

Intensity function is the measured signal. The result from Eq. (4.26) coincides with the intensity dependence for the scanning microscopy (Sheppard and Wilson, 1978).

4.4 General description

It is apparent that the signal and the spectral density are related to each other. The measurement uncertainty is calculated from the signal $I(\theta)$ by means of Eq. (4.5). The standard deviation of the wave number is calculated from the normalized spectral density $s(k_\theta)$. The quantity k_θ is the angular spatial frequency associated with the coordinate θ. In Eqs. (4.6) and (4.17), k_θ corresponds to a spatial component of the wave vector $\mathbf{k}$.

The signal (intensity) $I(\theta)$ is related to amplitude function $A(\theta)$ in a similar way as the spectral density $S(k_\theta)$ is related to amplitude spectral density $V(k_\theta)$ (Peřina, 1971)

$$I(\theta) = |A(\theta)|^2, \tag{4.27}$$

$$S(k_\theta) = |V(k_\theta)|^2. \tag{4.28}$$

The relation between $S(k_\theta)$ and $s(k_\theta)$ is given by

$$s(k_\theta) = \frac{S(k_\theta}{\int\limits_{-\infty}^{\infty} dk_\theta S(k_\theta)}. \tag{4.29}$$

The amplitude spectral density is connected with the amplitude function by Fourier transform

$$V(k_\theta) = \int\limits_{-\infty}^{\infty} d\theta A(\theta) \exp(-ik_\theta\theta) = \mathcal{F}\{A(\theta)\}. \tag{4.30}$$

The reason why the path length p is chosen as the coordinate θ in Eq. (4.17) instead of the distance z is the agreement of Eq. (4.30) with variables k_{z1} and p.

The relation of quantities $I(\theta)$, $A(\theta)$, $V(k_\theta)$, and $S(k_\theta)$ is illustrated in Fig. 4.5. An example of the triplet $A(\theta)$, $I(\theta)$, and $s(k_\theta)$ is represented by Eqs. (4.17), (4.18), and (4.20).

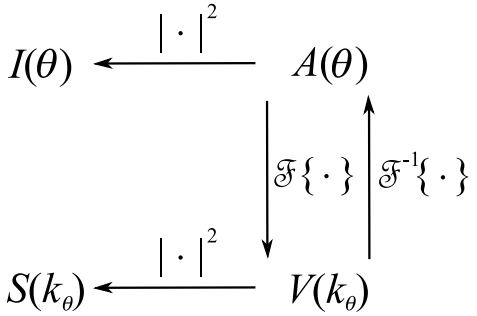

Figure 4.5: The relation of quantities $I(\theta)$, $A(\theta)$, $V(k_\theta)$, and $S(k_\theta)$.

The uncertainty of parameter a can be calculated by inserting $A(\theta, a)$ into Eq. (4.5)

$$(\delta a)^2 = \frac{\int\limits_{-\infty}^{\infty} d\theta |A(\theta,a)|^2}{N_{\text{all}} \int\limits_{-\infty}^{\infty} d\theta \left[\frac{\partial}{\partial a}(|A(\theta,a)|^2)/|A(\theta,a)|\right]^2}. \tag{4.31}$$

Equation (4.31) can be further simplified, if the amplitude function is real up to a multiplicative factor

$$A(\theta, a) = \beta A_R(\theta, a). \tag{4.32}$$

The function $A_R(\theta, a)$ is real and β can be expressed as

$$\beta = \exp[i(k_S\theta + \varphi_0)], \tag{4.33}$$

where k_S is a constant angular spatial frequency and φ_0 is phase constant.

Then, Eq. (4.31) takes the form

$$(\delta a)^2 = \frac{\int\limits_{-\infty}^{\infty} d\theta [A_R(\theta, a)]^2}{4N_{\text{all}} \int\limits_{-\infty}^{\infty} d\theta \left[\frac{\partial}{\partial a} A_R(\theta, a)\right]^2}. \tag{4.34}$$

The amplitude spectral density is equal to

$$V(k_\theta) = \exp(-i\varphi_0)\mathcal{F}\{A_R(\theta, a)\}(k_\theta - k_S). \tag{4.35}$$

Because $A_R(\theta, a)$ is a real function, $V(k_\theta)$ is symmetric and shifted by k_S. For example, the shift is equal to $k_S = (k_1 + k_2)/2$ in the case of two-slit device as follows from Eq. (4.20) and Fig. 4.4(b).

The standard deviation of k_θ can be calculated by means of Eqs. (4.28) and (4.30).

$$(\delta k_\theta)^2 = \frac{\int\limits_{-\infty}^{\infty} dk_\theta |\mathcal{F}\{A_R(\theta, a)\}|^2 k_\theta^2}{\int\limits_{-\infty}^{\infty} dk_\theta |\mathcal{F}\{A_R(\theta, a)\}|^2}. \tag{4.36}$$

The function $g(\theta, a)$ from Eq. (4.2) has usually the form $g(\theta - a)$ as can be seen in Eqs. (4.7) and (4.18). Then, $\partial g/\partial\theta = -\partial g/\partial a$ and it holds according to Plancherel's theorem

$$\int\limits_{-\infty}^{\infty} d\theta [A_R(\theta, a)]^2 = \int\limits_{-\infty}^{\infty} dk_\theta |\mathcal{F}\{A_R(\theta, a)\}|^2. \tag{4.37}$$

Similarly, it holds

$$\int\limits_{-\infty}^{\infty} dk_\theta |\mathcal{F}\{A_R(\theta, a)\}|^2 k_\theta^2 = \int\limits_{-\infty}^{\infty} d\theta \left[\frac{\partial}{\partial a} A_R(\theta, a)\right]^2. \tag{4.38}$$

The uncertainty product is calculated by use of Eqs. (4.34), (4.36), (4.37), and (4.38)

$$\delta a \cdot \delta k_\theta = \frac{1}{2\sqrt{N_{\text{all}}}}. \tag{4.39}$$

As expected, the result given by Eq. (4.39) coincides with those of Eqs. (4.9) and (4.21).

4.5 Derivation without quantum theory

Equation (4.5) contains the number N_{all} of photocounts detected in all samples. Thus, it would seem that Eq. (4.5) has to be derived using methods of quantum optics. However, the equation for calculating the measurement uncertainty can be derived from simple assumptions.

In a CCD detector, the number of photons is converted to a charge and subsequently the charge is converted to voltage. A CCD camera consists of a CCD chip and associated electronics, which is used to amplify the voltage on the CCD, digitise the pixel values and output the values of each pixel to a PC. The intensity of light in a given pixel is expressed by a number n_{DN}. DN states for digital number. For example, the number n_{DN} is in the range of 0 to 4095 for a 12-bit CCD camera.

The signal is then described by

$$(n_{\mathrm{DN}})_j \quad \text{for} \quad j = 0 \ldots M-1 \tag{4.40}$$

for discrete values or by

$$n_{\mathrm{DN}}(x) \quad \text{for} \quad x \in [x_1, x_2] \tag{4.41}$$

for continuous values.

It is mentioned in Section 3.1 that we need to know two items of the information for the application of the Cramér-Rao inequality. They are the analytical description of the model signal and the probability density function of the noise.

The analytical description of the model signal is known for the individual methods. Examples of the signal are given in Eqs. (4.6), (4.18), (4.22), and (4.26).

Concerning the noise, the light of lasers obeys Poisson photocount distribution. However, for large intensities (such as those used for practical measurements) Poisson distribution can be approximated by normal distribution with mean $\langle n_{\mathrm{DN}} \rangle$ and variance $(\Delta n_{\mathrm{DN}})^2$. The variance is directly proportional to the mean

$$(\Delta n_{\mathrm{DN}})^2 = \kappa \langle n_{\mathrm{DN}} \rangle, \tag{4.42}$$

where κ is a proportionality constant. Equation (4.42) is analogy of Eq. (4.1).

In this case, the Cramér-Rao inequality gives the result (for the case of equality)

$$(\delta a)^2 \approx \kappa \left\{ \sum_{i=0}^{M-1} \left[\left(\frac{\partial n_{\mathrm{DN}}(a, x_i)}{\partial a} \right)^2_{x=x_i} \frac{1}{n_{\mathrm{DN}}(a, x_i)} \right] \right\}^{-1}. \tag{4.43}$$

Equation (4.43) is equivalent to Eq. (4.2). The meaning of $n_{\mathrm{DN}}(x, a)$ and $\partial n_{\mathrm{DN}}(x, a)/\partial a$ follows from Fig. 4.6.

Note: In Eq. (4.43), the approximation sign is used instead of the equal sign. This is because in addition to the term on the right side of Eq. (4.43), an additional term appears in the result. The additional term is smaller than the listed term in a ratio equal to $1 : [2\ (\mathrm{SNR})^2]$, where SNR is signal to noise ratio. Thus, for usual values of intensity, the additional term may be neglected.

The only quantum assumption in the above derivation is Eq. (4.42). This equation can be considered as one of the heads of atomic phenomena, as Lederman and Hill (2011) write about them [1].

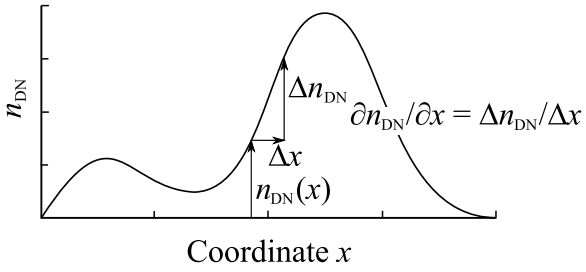

Figure 4.6: An example of a signal $n_{\mathrm{DN}}(x)$. Meaning of quantities $n_{\mathrm{DN}}(x, a)$ and $\partial n_{\mathrm{DN}}(x, a)/\partial x$.

4.6 Summary

The measurement uncertainty has been calculated for the case of an optically smooth surface. In this case, shot noise can be considered as the dominant source of noise. The measurement uncertainty has been calculated for two strongly simplified models of optical 3D sensors. The first model represents a deflectometer while the second can be considered as a model of the focus sensor and, with some variation, of the classical interferometer. The calculations have shown that in both cases an uncertainty product can be found that combines the measurement uncertainty and the standard deviation of the spectral density. It has also been indicated how it is possible to switch from simplified models to usual optical sensors. Finally, general rules have been found that apply to the generation of the uncertainty product. This chapter is based on the following publications:

[A5] Pavlíček, P. and M. Pech (2016). Shot noise limit of the optical 3D measurement methods for smooth surfaces. *Measurement Science and Technology 27*(3), 035205.

[1] L. M. Lederman and C. T. Hill write in the mentioned book: "We should not be surprised that atomic phenomena can occasionally rear their heads in the macroscopic world of people and their measuring instruments."

[A6] Pavlíček, P. (2014). Optical methods for the measurement of the shape of objects and their measurement uncertainty. In *SPIE 9441*, pp. 94411K.

[A7] Pavlíček, P. and G. Häusler (2014). Methods for optical shape measurement and their measurement uncertainty. *International Journal of Optomechatronics 8*(4), 292—303.

Chapter 5

Measurement uncertainty on optically rough surfaces

As an example of uncertainty on rough surface, the measurement uncertainty of coherence-scanning interferometry is mentioned. The dominant noise of coherence-scanning interferometry on rough surface is the influence of surface roughness (Häusler and Ettl, 2011; Pavlíček, 2011). This kind of noise is also referred to as object noise.

5.1 Measurement uncertainty

A typical setup for coherence-scanning interferometry on rough surfaces is shown in Fig. 5.1. The measured object with the rough surface is placed in one arm of Michelson interferometer. The object is moved during the measurement and an interferogram is recorded in each pixel of CCD camera. Because of the rough surface, the phase of the interferogram is not evaluated. The position at which the interferometer is balanced is determined from the maximum position of the interferogram envelope. The Hilbert transform is used as a standard tool for calculating the interferogram envelope (Pavlíček and Svak, 2015).

The rough surface is considered as a set of scattering centers with randomly varying height and reflectivity (Goodman, 1984, 2008). When objects with optically rough surfaces are measured, a speckle pattern arises in the image plane. The goal is to find the distribution of the measurement error caused by the surface roughness. Based on this knowledge, the measurement uncertainty is determined [A9] (Pavlíček and Hýbl, 2008).

The measurement error is calculated with following assumptions:

1. A planar rough surface is considered.
2. The resolution cell of the imaging system contains N scattering centers.

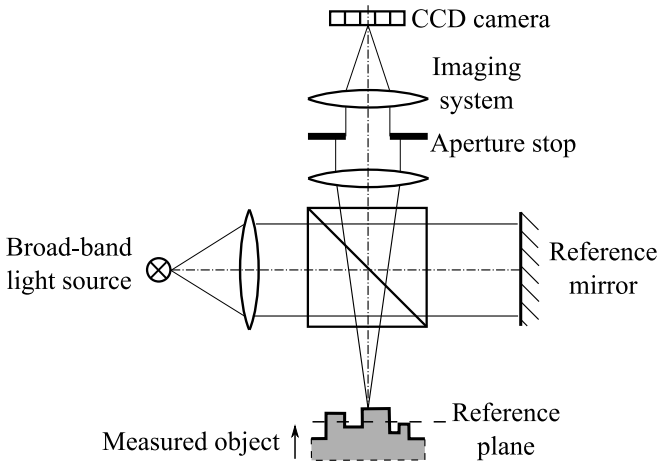

Figure 5.1: Setup for coherence-scanning interferometry on rough surface.

3. Height h_j of the jth scattering center is a random variable obeying a Gaussian distribution with zero mean. Standard deviation σ_h of the height distribution is equal to quadratic roughness (Nieto-Vesperinas, 2006).

4. Without loss of generality, we may assume that the reflectivity of all scattering centers is equal to 1 (Goodman, 1984).

5. The spectral density of the broad-band light source has a Gaussian form

$$S(k) = \frac{1}{2\sqrt{\pi}\Delta k} \exp\left[-\left(\frac{k-k_0}{2\Delta k}\right)^2\right], \tag{5.1}$$

where k_0 is the central wave number and Δk is the effective band width [A8] (Pavlíček and Soubusta, 2003).

In practice, the spectral width is usually expressed in wavelength units. The relation between effective band width Δk and the full width at half maximum (FWHM) in wavelength units is given by [A8] (Pavlíček and Soubusta, 2003)

$$\begin{aligned} \Delta k &= 4\frac{\pi}{\sqrt{\ln 2}} \frac{1}{\mathrm{FWHM}(\lambda)} \left[\sqrt{1+\left(\frac{\mathrm{FWHM}(\lambda)}{\lambda}\right)^2} - 1\right] \\ &\approx \frac{\pi}{2\sqrt{\ln 2}} \frac{\mathrm{FWHM}(\lambda)}{\lambda^2}. \end{aligned} \tag{5.2}$$

The fact that FWHM is expressed in wavelength units is indicated by the symbol λ in parentheses. The coherence length of the light source with

the spectrum described by Eq. (5.1) is given by

$$l_c = \frac{1}{2\Delta k} \approx \frac{\sqrt{\ln 2}}{\pi} \frac{\lambda^2}{\mathrm{FWHM}(\lambda)}. \tag{5.3}$$

The interferogram for monochromatic light with wave number k is given by [A10] (Pavlíček, 2008)

$$I(z) = \underbrace{C^2 + S^2 + B^2}_{\text{offset}} + \underbrace{2B(C\cos 2kz + S\sin 2kz)}_{\text{modulation part}}. \tag{5.4}$$

The meaning of the symbols used in Eq. (5.4) is as follows

$$C = \sum_{i=0}^{N-1} \cos 2kh_i, \tag{5.5}$$

$$S = \sum_{i=0}^{N-1} \sin 2kh_i, \tag{5.6}$$

and B is the amplitude of the reference wave.

The modulation part for polychromatic light is given by integration over the spectrum of the light source

$$I_{\mathrm{mod}} = \int_0^\infty dk\ S(k)\, 2B(C\cos 2kz + S\sin 2kz). \tag{5.7}$$

The integration can be carried out

$$I_{\mathrm{mod}} = 2B \sum_{i=0}^{N-1} \exp[-4(z-h_i)^2(\Delta k)^2] \cos 2k_0(z-h_i). \tag{5.8}$$

The square of the envelope of the interferogram can be expressed by

$$E^2 = 4B^2 \sum_{i=0}^{N-1} \sum_{j=0}^{N-1} \exp\{-4[(z-h_i)^2+(z-h_j)^2](\Delta k)^2\} \cos 2k_0(h_i-h_j). \tag{5.9}$$

It follows from Eq. (5.4) that the intensity of a speckle with shut reference arm ($B = 0$, the object arm only is open) is given by

$$I_{\mathrm{obj}} = C^2 + S^2 = \sum_{i=0}^{N-1} \sum_{j=0}^{N-1} \cos(\varphi_i - \varphi_j) \tag{5.10}$$

with $\varphi_i = 2k_0h_i$. The mean value of I_{obj} is equal to

$$\langle I_{\mathrm{obj}} \rangle = N. \tag{5.11}$$

The position z_e of the maximum of the envelope can be calculated from the condition $\partial E/\partial z = 0$ that is equivalent to $\partial E^2/\partial z = 0$. It follows from Eq. (5.9)

$$z_e \approx \frac{\sum_{i=0}^{N-1}\sum_{j=0}^{N-1}(h_i + h_j)\cos[2k_0(h_i - h_j)]}{2\sum_{i=0}^{N-1}\sum_{j=0}^{N-1}\cos[2k_0(h_i - h_j)]}. \tag{5.12}$$

The mean of the numerator of the expression in Eq. (5.12) is equal to zero. Thus, the variance is given by

$$\mathrm{var}(\text{numerator}) = \langle(\text{numerator})^2\rangle. \tag{5.13}$$

The angled brackets $\langle\,\rangle$ denote expected value. The expression $\langle(\text{numerator})^2\rangle$ is calculated using Eq. (5.11)

$$\begin{aligned}
\langle(\text{numerator})^2\rangle &= \left\langle \left[\sum_{i=0}^{N-1}\sum_{j=0}^{N-1}(h_i + h_j)\cos(\varphi_i - \varphi_j)\right]^2 \right\rangle \\
&= \sum_{i=0}^{N-1}\sum_{j=0}^{N-1}\sum_{k=0}^{N-1}\sum_{l=0}^{N-1}\langle(h_i + h_j)(h_k + h_l)\cos(\varphi_i - \varphi_j)\cos(\varphi_k - \varphi_l)\rangle \\
&= 4\sum_{i=0}^{N-1}\sum_{j=0}^{N-1}\sum_{k=0}^{N-1}\langle\cos(\varphi_i - \varphi_j)\cos(\varphi_i - \varphi_k)\rangle\sigma^2 \\
&= 2N\sum_{i=0}^{N-1}\sum_{j=0}^{N-1}\cos(\varphi_i - \varphi_j)\sigma^2 \\
&= 2\langle I_{\mathrm{obj}}\rangle I_{\mathrm{obj}}.
\end{aligned} \tag{5.14}$$

It follows from Eqs. (5.12), (5.10), and (5.14) that the standard deviation of the position z_e is equal to

$$\delta(z_e) = \frac{1}{\sqrt{2}}\sqrt{\frac{\langle I_{\mathrm{obj}}\rangle}{I_{\mathrm{obj}}}}\sigma_h. \tag{5.15}$$

The result given by Eq. (5.15) is the same as that derived by Dresel (1991). However the way of derivation presented here is different from that performed by Dresel.

Equation (5.15) shows that for bright speckles, the measurement uncertainty is lower. Wiesner et al. (2012) introduced the idea of creating multiple speckle fields using light sources with different wavelengths. At each point of the measured surface, the brightest speckle is then selected for evaluation.

5.2 Distorted interferograms

George and Jain have demonstrated that speckle patterns of two different wavelengths become decorrelated if the surface roughness exceeds a certain

limit (George and Jain, 1973). Speckle pattern produced by broad band light can also be expected to be decorrelated if the surface is too rough. The goal is to find a similar limit for broad-band illumination. The knowledge of such a roughness limit is important for practical measurements because the interferogram obtained from a decorrelated speckle pattern is distorted and it is difficult to evaluate it correctly.

As an example, a measured distorted interferogram for $\lambda = 820$ nm, FWHM(λ) = 44 nm ($l_c = 4.1$ μm), $Ra = 1.6$ μm ($\sigma_h \approx 2.0$ μm), and $I_{\mathrm{out\,obj}}/\langle I_{\mathrm{out\,obj}}\rangle = 1.2$ is shown in Fig. 5.2(a). It is difficult to evaluate such a distorted interferogram correctly. For instance, if we use the maximum (Saraç et al., 2004) or the center of gravity (Recknagel and Notni, 1998) of the interferogram's envelope as the indicator of the balance of the interferometer, we obtain two different values, as shown in Fig. 5.2(a).

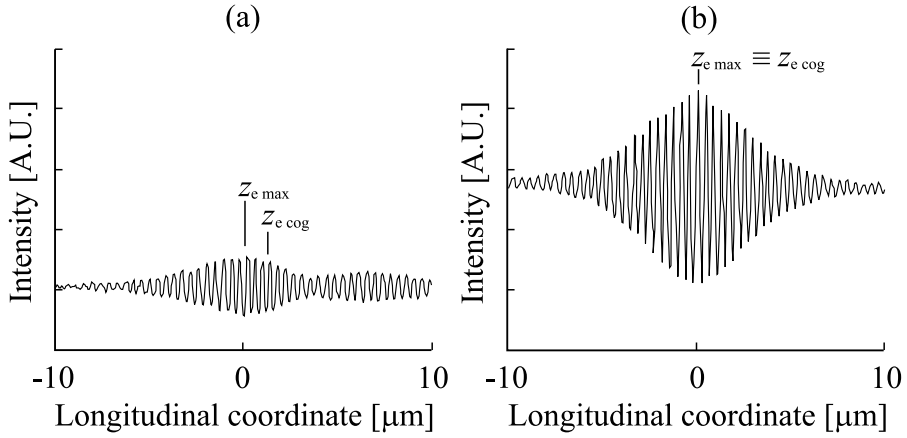

Figure 5.2: Example of measured interferograms. $\lambda = 820$ nm, FWHM(λ) = 44 nm, $Ra = 1.6$ μm. (a) Distorted interferogram. (b) Undistorted interferogram.

On the other hand, the different results provided by the different evaluation methods can be used as a decision criterion whether the interferogram is distorted or not [A9] (Pavlíček and Hýbl, 2008). Let us denote

$$\Delta_{\mathrm{form}} = z_{\mathrm{e\,max}} - z_{\mathrm{e\,cog}}, \tag{5.16}$$

where $z_{\mathrm{e\,max}}$ is the position of the maximum of the calculated interferogram's envelope, as described in Section 5.1, and $z_{\mathrm{e\,cog}}$ is the position of the center of gravity of the interferogram's envelope. The meaning of $z_{\mathrm{e\,max}}$ and $z_{\mathrm{e\,cog}}$ is illustrated in Fig. 5.2(a).

The numerically calculated distribution of difference Δ_{form} for FWHM(λ) = 38 nm, $\sigma_h = 1.2$ μm, and $I_{\mathrm{out\,obj}} = \langle I_{\mathrm{out\,obj}}\rangle$ is depicted in Fig. 5.3 as an example. The distribution has been estimated based on 40 000 simulations.

The number of scattering regions $N = 200$. It turns out that the distribution of Δ_{form} does not approach a Gaussian form. Numerical simulations show that the shape of the distribution of Δ_{form} is more like a truncated zero-mean Lorentzian distribution. The shape of the truncated Lorentzian distribution is plotted by the dashed curve in Fig. 5.3.

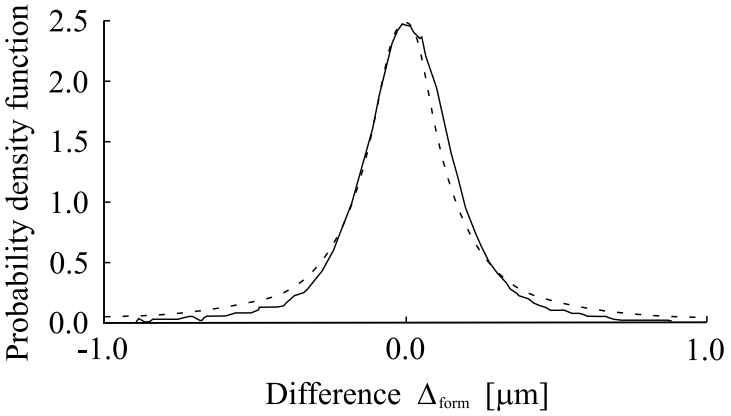

Figure 5.3: Example of the numerically calculated distribution of Δ_{form}.

It is useful to set a criterion by which to decide whether the interferogram is distorted or not. The numerical calculations show that standard deviation σ_Δ of the distribution of Δ_{form} is increasing with increasing spectral width FWHM(λ). A suitable decision criterion for an undistorted interferogram seems to be the condition that the standard deviation σ_Δ does not exceed one-third of δz as defined by Eq. (5.15) for the given roughness σ_h and intensity $I_{\text{out obj}}$. In this way, the limit spectral width FWHM_{lim} can be calculated.

If $\text{FWHM}(\lambda) = \text{FWHM}_{\text{lim}}$, the numerical calculations show that the probability that the difference Δ_{form} exceeds the theoretical value δ_z is about 0.018. If the distribution of Δ_{form} had a Gaussian form, the probability would be 0.0027.

The limit spectral width FWHM_{lim} is numerically calculated for $\lambda_0 = 820$ nm and various values of roughness σ_h and intensity $I_{\text{out obj}}$. The result is presented in Fig. 5.4. The marks in Fig. 5.4 indicate the numerically calculated values of the limit spectral width FWHM_{lim}. The dashed curves represent the values calculated according to the formula

$$l_{\text{c lim}} = 4\sqrt{\frac{\langle I_{\text{out obj}}\rangle}{I_{\text{out obj}}}}\sigma_h. \tag{5.17}$$

The relation between the limit coherence length $l_{\text{c lim}}$ and the limit spectral width FWHM_{lim} is expressed by Eq. (5.3).

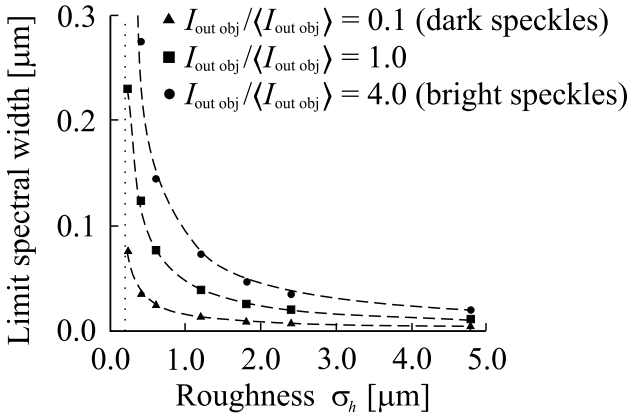

Figure 5.4: Limit spectral width $\mathrm{FWHM_{lim}}$ as the function of roughness σ_h. The marks indicate the numerically calculated values. The dashed curves represent the values calculated according to Eq. (5.17).

The numerically calculated values of the limit spectral width $\mathrm{FWHM_{lim}}$ tend, approximately, to the values given by Eq. (5.17) as follows from Fig. 5.4. The limit spectral width is increasing with intensity $I_{\text{out obj}}$ and decreasing with roughness σ_h. The area that is enclosed by the calculated values of the limit spectral width $\mathrm{FWHM_{lim}}$, the horizontal axis, and the dotted line $\sigma_h = \lambda_0/4$ (the approximate limit of the optically rough surface) represents the application range where undistorted interferograms may be expected. The described application range is larger for the speckles with a higher intensity $I_{\text{out obj}}$.

This corresponds to experience with practical measurements as shown in Fig. 5.2 . Two measured interferograms for $\lambda_0 = 820$ nm and FWHM(λ) = 44 nm are presented. The measured object is roughness standard (N7 Rugotest number 3) with $Ra = 1.6$ μm (Ettl et al., 1998). For a Gaussian height distribution, it holds $Ra = (2/\pi)^{1/2}\sigma_h \approx 0.8\,\sigma_h$ (Lehmann, 2002). Thus σ_h takes, approximately, the value of 2.0 μm. The values of the ratio $I_{\text{out obj}}/\langle I_{\text{out obj}}\rangle$ are 1.2 and 4.5 for the interferograms shown in Figs. 5.2 (a) and Fig. 5.2(b), respectively.

The limit spectral width is equal to 24 nm for the interferogram in Fig. 5.2(a). The interferogram illustrated in Fig. 5.2(a) is distorted because the spectral width (44 nm) of the light source exceeds the limit spectral width (24 nm). On the other hand, the limit spectral width for the interferogram in Fig. 5.2(b) is 47 nm. In this case, the limit spectral width is not exceeded by the spectral width (44 nm) of the light source, and therefore the interferogram illustrated in Fig. 5.2(b) is not distorted. This shows that the speckles with higher intensity are less sensitive to decorrelation. However, the speckles with higher intensity have a lower occurrence probability

according to the intensity distribution (Goodman, 1984).

Figure 5.5 shows the measurement uncertainty numerically calculated from the envelope maximum (denoted as δ_{Xz}) and the measurement uncertainty numerically calculated from the center of gravity (denoted as δ_{Gz}) of the interferogram's envelope as a function of spectral width FWHM(λ) for $\lambda = 820$ nm, $\sigma_h = 1.2$ μm, and $I_{\text{out obj}} = \langle I_{\text{out obj}} \rangle$.

As expected, both measurement uncertainties δ_{Xz} and δ_{Gz} take almost the same value for small spectral widths FWHM(λ). Because the interferograms are undistorted for small values of FWHM(λ). The value $\delta_z = \delta_{Xz} = \delta_{Gz}$ is given by Eq. (5.15) and is indicated by the horizontal dashed line in Fig. 5.5. If the spectral width is increased, both measurement uncertainties δ_{Xz} and δ_{Gz} start to differ from each other. The reason for this difference is that for very short coherence lengths ($l_c < 1\mu$m) δ_{Xz} maintains approximately the same value as before, whereas δ_{Gz} tends to zero. The value of the limit spectral width FWHM_{lim} is indicated by the vertical dotted line in Fig. 5.5. It can be seen that for this spectral width the difference between uncertainties δ_{Xz} and δ_{Gz} starts to increase.

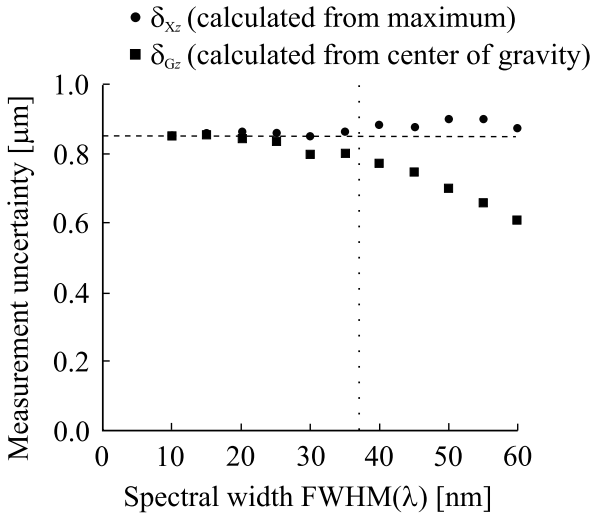

Figure 5.5: Measurement uncertainty as function of spectral width FWHM(λ).

It might seem more advantageous to use just distorted interferograms when their measurement uncertainty is less than those undistorted. The problem is that the influence of the rough surface only is taken into account in the presented theory. Other sources of noise will not allow accurate measurement of the shape of the distorted interferogram. However, this is necessary for an accurate coordinate calculation using the center of gravity method.

5.3 Summary

Coherence-scanning interferometry has been chosen as an example for calculating the measurement uncertainty on a rough surface. In this case, surface roughness is the dominant source of noise. The rough surface leads to the formation of speckle pattern. Measurement uncertainty is low in bright speckles and high in dark speckles. High roughness and large width of the light spectrum lead to the formation of distorted interferograms. Bright speckles are more resistant to the formation of distorted interferograms. The content of the chapter draws from the following publications:

[A8] Pavlíček, P. and J. Soubusta (2003). Theoretical measurement uncertainty of white-light interferometry on rough surfaces. *Applied Optics 42*(10), 1809–1813.

[A9] Pavlíček, P. and O. Hýbl (2008). White-light interferometry on rough surfaces—measurement uncertainty caused by surface roughness. *Applied Optics 47*(16), 2941–2949.

[A10] Pavlíček, P. (2008). Influence of surface roughness on the measurement uncertainty of white-light interferometry. In *SPIE 7141*, pp. 71410R.

Chapter 6

Conclusion

The measurement uncertainty of optical 3D sensors depends on whether the surface of the measured object is optically smooth or rough. The property of a surface to be optically smooth or rough depends on the mechanical properties of the surface and on the parameters of the optical measuring system. In the presented model, the mechanical properties of the surface are the mechanical roughness and the correlation length. The parameters of the optical measuring system are the wavelength of the used light and the aperture of the imaging system.

A surface behaves as optically rough if the roughness is large and the correlation length and aperture are small. An optical sensor operates in "rough surface mode" or "unresolved mode". As the roughness decreases and the correlation length and aperture increase, the surface becomes optically smooth. The optical sensor then operates in "smooth surface mode" or "resolved mode". When switching from "unresolved mode" to "resolved mode", the sensor goes through a transient range.

An optical sensor can operate in "resolved mode" even if the mechanical roughness is high. This is the case if the dimensions of the resolution cell of the optical system are less than the correlation length of the surface.

Whether the sensor operates in "resolved mode" or "unresolved mode" is important in terms of signal formation. The way the signal is generated depends on the dominant noise. Thus, the dominant type of noise is decisive in determining the measurement uncertainty of a particular sensor. Cramér–Rao inequality proves to be a suitable tool for calculating the measurement uncertainty [A1–A3]. For shot noise, Cramér–Rao inequality takes on a simple form [A4].

We assume that the shot noise is the dominant noise source for optical sensors operating on the optically smooth surface [A7]. The measurement uncertainty of several simplified model methods has been calculated by means of the Cramér–Rao inequality [A5].

It shows up that the measurement uncertainty of the measurement me-

thods on the optically smooth surface depends on the wavelength of used light, on the number of photons used for the measurement, and on the geometric arrangement of the measurement setup [A6].

One physical principle is common to all studied methods (laser deflectometry, classical interferometry, optical focus sensor). The product of the measurement uncertainty with the standard deviation of normalized spectral density cannot fall below a minimum achievable value. This value depends only on the number of photons used for the measurement. The condition to achieve the minimum value of the product is that the amplitude function must be real up to a multiplicative factor. The existence of the uncertainty product implies that a low measurement uncertainty can be achieved at the cost of large standard deviation of the normalized spectral density [A5].

For optical sensors that measure on optically rough surfaces, shot noise does not play a major role, one of the other sources of noise becomes dominant. The measurement uncertainty of coherence scanning interferometry has been given as an example for the measurement on optically rough surfaces. The influence of surface roughness is the dominant noise source in this case [A8].

Because of the great complexity, most of the problem has been solved numerically. The numerical calculations have shown that coherence-scanning interferometry on optically rough surface can operate in two regimes. These are: the regime with an undistorted interferogram and the regime with a distorted interferogram [A9]. The boundary between them is defined by the "limit spectral width" [A10]. If the spectral width of the light source is smaller than the limit spectral width, the interferogram is not distorted.

References

Abramowitz, M. and I. A. Stegun (1970). *Handbook of Mathematical Functions*. New York: Dover Publications, Inc.

Albrecht, H. E., M. Borys, N. Damaschke, and C. Tropea (2003). *Laser Doppler and Phase Doppler Measurement Techniques*. Berlin: Springer.

Da Costa, G. and G. Guerri (1978). Statistical distribution of the phase in noncircular Gaussian speckle patterns. *Journal of Optical Society of America 68*(6), 866–867.

Dorsch, R., G. Häusler, and J. M. Herrmann (1994). Laser triangulation: fundamental uncertainty in distance measurement. *Applied Optics 33*(7), 1306–1314.

Drabarek, P. (2001). Interferometric measuring device. Patent EU 2001, EP 1337803 B1.

Dresel, T. (1991). Grundlagen und Grenzen der 3D-Datengewinnung mit dem Kohärenzradar. Master's thesis, University Erlangen – Nuremberg, Erlangen, Germany.

Dresel, T., G. Häusler, and H. Venzke (1992). Three-dimensional sensing of rough surface by coherence radar. *Applied Optics 31*(7), 919–925.

Ettl, P., B. Schmidt, M. Schenk, I. Laszlo, and G. Häusler (1998). Roughness parameters and surface deformation measured by 'Coherence Radar'. In *SPIE 3407*, pp. 133–140.

Falconi, O. (1964). Maximum sensitivities of optical direction and twist measuring instruments. *Journal of the Optical Society of America 54*(11), 1315–1320.

Fischer, A. (2019). Limiting uncertainty relations in laser-based measurements of position and velocity due to quantum shot noise. *Entropy 21*(3), 264.

Fox, M. (2006). *Quantum Optics: An Introduction*. Oxford UK: Oxford University Press.

George, N. and A. Jain (1973). Speckle reduction using multiple tones of illumination. *Applied Optics 12*(6), 1202–1212.

Goodman, J. W. (1984). Statistical properties of laser speckle patterns. In J. C. Dainty (Ed.), *Laser Speckle and Related Phenomena*, pp. 9–75. Berlin: Springer Verlag.

Goodman, J. W. (2005). *Introduction to Fourier Optics*. Greenwood Village CO: Roberts & Company Publishers.

Goodman, J. W. (2008). Speckle with finite number of steps. *Applied Optics 47*(4), A111–A118.

Guide to expression of uncertainty in measurement (2016). Available at `http://www.bipm.org/en/publications/guides/gum.html` (2021/02/01).

Häusler, G. (1999). Verfahren und Vorrichtung zur Ermittlung der Form oder der Abbildungseigenschaften von spiegelnden oder transparenten Objekten. Patent DE 1999, 19944354 A1.

Häusler, G., P. Ettl, M. Schenk, G. Bohn, and I. Laszlo (1999). Limits of optical range sensors and how to exploit them. In T. Asakura (Ed.), *International Trends in Optics and Photonics ICO IV*, pp. 328–342. Berlin: Springer Verlag.

Häusler, G. and S. Ettl (2011). Limitations of optical 3D sensors. In R. Leach (Ed.), *Optical Measurement of Surface Topography*, pp. 23–48. Berlin: Springer Verlag.

Kino, G. S. and S. S. C. Chim (1990). Mirau correlation microscope. *Applied Optics 29*(26), 3775–3783.

Knauer, M. C., J. Kaminski, and G. Häusler (2004). Phase measuring deflectometry: a new approach to measure specular free-form surfaces. In *SPIE 5457*, pp. 366 – 376.

Kubáček, L. (1988). *Foundations of Estimation Theory*. Amsterdam: Elsevier.

Lauterborn, W., T. Kurz, and M. Wiesenfeldt (1995). *Coherent Optics*. Berlin: Springer.

Lederman, L. M. and C. T. Hill (2011). *Quantum Physics for Poets*. Amherst: Prometheus Books.

Lehmann, P. (2002). Aspect ratio of elongated polychromatic far-field speckles of continuous and discrete spectral distribution with respect to surface roughness characterization. *Applied Optics 41*(10), 2008–2014.

Loudon, R. (2000). *The Quantum Theory of Light*. Oxford: Oxford University Press.

Nayar, S. K. and Y. Nakagawa (1994). Shape from focus. *IEEE Transactions on Pattern Analysis and Machine Intelligence 16*(8), 824–831.

Nieto-Vesperinas, M. (2006). *Scattering and Diffraction in Physical Optics*. Singapore: World Scientific.

Pavlíček, P. (2008). Influence of surface roughness on the measurement uncertainty of white-light interferometry. In *SPIE 7141*, pp. 71410R.

Pavlíček, P. (2011). Measurement uncertainty of white-light interferometry on optically rough surfaces. In J. Awrejcewicz (Ed.), *Numerical Simulations of Physical and Engineering Processes*, pp. 491–502. Rijeka: InTech.

Pavlíček, P. (2014). Optical methods for the measurement of the shape of objects and their measurement uncertainty. In *SPIE 9441*, pp. 94411K.

Pavlíček, P. (2021). Optically smooth and optically rough surfaces in 3D profilometry. (submitted).

Pavlíček, P. and G. Häusler (2014). Methods for optical shape measurement and their measurement uncertainty. *International Journal of Optomechatronics 8*(4), 292–303.

Pavlíček, P. and O. Hýbl (2008). White-light interferometry on rough surfaces—measurement uncertainty caused by surface roughness. *Applied Optics 47*(16), 2941–2949.

Pavlíček, P. and O. Hýbl (2012). White-light interferometry on rough surfaces——measurement uncertainty caused by noise. *Applied Optics 51*(4), 465–473.

Pavlíček, P. and V. Michálek (2012a). White-light interferometry - envelope detection by Hilbert transform and influence of noise. *Optics and Lasers in Engineering 50*(8), 1063–1068.

Pavlíček, P. and V. Michálek (2012b). White-light interferometry, Hilbert transform, and noise. In *SPIE 8697*, pp. 86970B.

Pavlíček, P. and M. Pech (2016). Shot noise limit of the optical 3D measurement methods for smooth surfaces. *Measurement Science and Technology 27*(3), 035205.

Pavlíček, P. and J. Soubusta (2003). Theoretical measurement uncertainty of white-light interferometry on rough surfaces. *Applied Optics 42*(10), 1809–1813.

Pavlíček, P. and V. Svak (2015). Noise properties of Hilbert transform evaluation. *Measurement Science and Technology 26*(8), 085207.

Peřina, J. (1971). *Coherence of Light*. London UK: Van Nostrand Reinhold Company.

Recknagel, R. J. and G. Notni (1998). Analysis of white light interferograms using wavelet methods. *Optics Communications 148*(1–3), 122–128.

Riley, K. F., M. P. Hobson, and S. J. Bence (2004). *Mathematical Methods for Physics and Engineering*. Cambridge UK: Cambridge University Press.

Ronchi, V. (1961). Resolving power of calculated and detected image. *Applied Optics 51*(4), 458–460.

Saraç, Z., R. Groß, C. Richter, B. Wiesner, and G. Häusler (2004). Optimization of white light interferometry on rough surfaces based on error analysis. *Optik 115*(8), 351–357.

Schmit, J., K. Creath, and J. C. Wyant (2007). Surface profilers, multiple wavelength, and white-light interferometry. In D. Malacara (Ed.), *Optical Shop Testing*, pp. 667–755. New York: Wiley.

Sheppard, C. J. R. and T. Wilson (1978). Depth of field in the scanning microscopy. *Optics Letters 3*(3), 115–117.

Ulrich, R. and A. Koch (1992). Faseroptischer Antastsensor für rauhe Oberflächen. *Feinwerktechnik und Messtechnik F & M 100*(11), 521–524.

Vencálek, O. (2018). Private communication.

Whitehouse, D. J. (1994). *Handbook of Surface Metrology*. Bristol: IOP Publishing.

Wiesner, B., O. Hýbl, and G. Häusler (2012). Improved white-light interferometry on rough surfaces by statistically independent speckle patterns. *Applied Optics 51*(6), 751–757.

Supplementary material

The thesis draws material from the following ten articles published between years 2003-2016:

[A1] Pavlíček, P. and V. Svak (2015). Noise properties of Hilbert transform evaluation. *Measurement Science and Technology 26*(8), 085207.

[A2] Pavlíček, P. and V. Michálek (2012a). White-light interferometry–envelope detection by Hilbert transform and influence of noise. *Optics and Lasers in Engineering 50*(8), 1063—1068.

[A3] Pavlíček, P. and V. Michálek (2012b). White-light interferometry, Hilbert transform, and noise. In *SPIE 8697*, pp. 86970B.

[A4] Pavlíček, P. and O. Hýbl (2012). White-light interferometry on rough surfaces——measurement uncertainty caused by noise. *Applied Optics 51*(4), 465—473.

[A5] Pavlíček, P. and M. Pech (2016). Shot noise limit of the optical 3D measurement methods for smooth surfaces. *Measurement Science and Technology 27*(3), 035205.

[A6] Pavlíček, P. (2014). Optical methods for the measurement of the shape of objects and their measurement uncertainty. In *SPIE 9441*, pp. 94411K.

[A7] Pavlíček, P. and G. Häusler (2014). Methods for optical shape measurement and their measurement uncertainty. *International Journal of Optomechatronics 8*(4), 292—303.

[A8] Pavlíček, P. and J. Soubusta (2003). Theoretical measurement uncertainty of white-light interferometry on rough surfaces. *Applied Optics 42*(10), 1809–1813.

[A9] Pavlíček, P. and O. Hýbl (2008). White-light interferometry on rough surfaces—measurement uncertainty caused by surface roughness. *Applied Optics 47*(16), 2941–2949.

[A10] Pavlíček (2008). Influence of surface roughness on the measurementuncertainty of white-light interferometry. In *SPIE 7141*, pp. 71410R.

Due to copyright, copies of the articles are not available in the online version of the thesis. The complete version of the work can be viewed at the Department of Science and Research of the Faculty of Science of Palacký University.